

A roadmap to cosmological parameter analysis with third-order shear statistics II: Analytic covariance estimate

Laila Linke¹, Sven Heydenreich¹, Pierre A. Burger¹, Peter Schneider¹

Argelander-Institut für Astronomie, Auf dem Hügel 71, 53121 Bonn, Germany
e-mail: llinke@astro.uni-bonn.de

Version December 9, 2022; received xxx, accepted yyy

ABSTRACT

Context. Third-order weak lensing statistics are a promising tool for cosmological analyses since they extract cosmological information in the non-Gaussianity of the cosmic large-scale structure. However, such analyses require precise and accurate models for the covariance of the statistics.

Aims. In this second paper of a series on third-order weak lensing statistics, we derive and validate an analytic model for the covariance of the third-order aperture statistics $\langle M_{\text{ap}}^3 \rangle$.

Methods. We derive the covariance model from a real-space estimator for $\langle M_{\text{ap}}^3 \rangle$, including the Gaussian and non-Gaussian parts. We validate the model by comparing it to estimates from simulated Gaussian random fields (GRF) and two sets of N -body simulations. Finally, we perform mock cosmological analyses with the model covariance and the simulation estimate to compare the resulting parameter constraints.

Results. We find good agreement between the analytic model and the simulations, both for the GRF and the N -body simulations. The figure-of-merit in the S_8 - Ω_m plane from our covariance model is within 3% of the one obtained from the simulated covariances. We also show that our model, which is based on an estimator using convergence maps, can be used to obtain upper and lower bounds for the covariance of an estimator based on three-point shear correlation functions. This second estimator is required to measure $\langle M_{\text{ap}}^3 \rangle$ in realistic survey data. In our derivation, we find that the covariance of $\langle M_{\text{ap}}^3 \rangle$ cannot be obtained from the bispectrum covariance and that it includes several ‘finite-field terms’ that do not scale with the inverse survey area.

Conclusions. Our covariance model is sufficiently accurate for analysing stage III surveys. Covariances for statistics in Fourier space cannot always be straightforwardly converted into covariance for real-space statistics. The modelling code is available at <https://github.com/sheydenreich/threepoint/releases>.

Key words. gravitational lensing – weak, cosmology – cosmological parameters, methods – statistical, methods – analytical, large-scale structure of Universe

1. Introduction

Using weak gravitational lensing of the cosmic large-scale structure (LSS) has become a precise and accurate method to infer cosmological parameters (Heymans et al. 2021, Hikage et al. 2019, Abbott et al. 2022). Weak lensing analyses have mainly concentrated on second-order statistics, such as shear two-point correlation functions or galaxy-galaxy-lensing. However, since the cosmic LSS is non-Gaussian, second-order statistics do not contain its total information content. To access the additional information, higher-order statistics (HOS) are needed. These HOS depend differently on cosmological parameters than second-order statistics, so they can be used to break degeneracies (Takada & Jain 2004, Kilbinger & Schneider 2005, Kayo et al. 2013) or constrain nuisance parameters like galaxy bias or intrinsic alignment (Pyne & Joachimi 2021, Troxel & Ishak 2012).

Many HOS have been suggested to complement second-order analyses, for example, peak statistics (Kacprzak et al. 2016, Zürcher et al. 2021, Martinet et al. 2021), density split statistics (Friedrich et al. 2018, Gruen et al. 2018, Burger et al. 2022), or persistent homology (Heydenreich et al. 2021, 2022a). Most of these statistics, though, cannot be modelled from analytical theories and instead need time-consuming realistic N -body simulations. Additionally, for many HOS, the measurement requires converting weak lensing shear estimates to mass convergence maps. This conversion becomes complicated in the presence of masks and for finite survey areas, which can lead to biased estimators (Seitz & Schneider 1996).

In this series of papers, we are considering the third-order aperture mass $\langle M_{\text{ap}}^3 \rangle$, which is not affected by these problems. It is linearly related to the third-order shear correlation functions Γ_i (Jarvis et al. 2004, Schneider et al. 2005), which can be directly measured in shear catalogues and converted into $\langle M_{\text{ap}}^3 \rangle$. This was demonstrated recently by Secco

et al. (2022), who measured $\langle M_{\text{ap}}^3 \rangle$ with high significance from the Dark Energy Survey Year 3 shear catalogues. Moreover, in contrast to many other HOS, $\langle M_{\text{ap}}^3 \rangle$ and Γ_i can be modelled analytically without relying directly on simulations.

There are several advantages to using $\langle M_{\text{ap}}^3 \rangle$ instead of Γ_i , among them that $\langle M_{\text{ap}}^3 \rangle$ compress the information in the Γ_i from a data vector with thousands of entries to one containing only tens of entries in a non-tomographic setup, and that the $\langle M_{\text{ap}}^3 \rangle$ have a clear separation into E - and B -modes, allowing for the detection of untreated systematic effects. Our goal is to lay the groundwork for a cosmological analysis with $\langle M_{\text{ap}}^3 \rangle$. Such an analysis requires two ingredients: A model of $\langle M_{\text{ap}}^3 \rangle$ and an estimate of its covariance matrix. The first ingredient is the subject of Heydenreich et al. (2022b, Paper I hereafter), where we present and test an analytic model of $\langle M_{\text{ap}}^3 \rangle$ based on the BiHalofit bispectrum model (Takahashi et al. 2020). Here, we are concerned with the second ingredient, which is the covariance.

The covariance of the estimator of a statistic can be obtained in two ways. The first possibility is applying the estimator to a large set of (quasi-)independent cosmological N -body simulations and using the sample covariance of the estimates. However, an unbiased and precise estimate requires many more realisations than entries in the data vector. For example, for a tomographic analysis of $\langle M_{\text{ap}}^3 \rangle$ with four redshift bins and four different scale radii, the data vector contains 400 entries, so hundreds of simulations are needed for a simulated covariance estimate. Such an estimate would be very time-consuming, as both the creation of this many independent simulations and the measurement of $\langle M_{\text{ap}}^3 \rangle$ in them is computationally demanding.

Instead, cosmic shear covariances can also be calculated analytically for a given estimator. This was done, for example, for two-point statistics (Joachimi et al. 2008) or the matter bispectrum (Joachimi et al. 2009). While the derivation of an expression for a covariance can be tedious, once it is done, evaluating them for the characteristics of a specific survey is usually accurate and quick, at least compared to running hundreds of cosmological simulations. It is also easier to infer the dependence of the covariance on survey area and geometry from an analytic expression. Consequently, we follow this approach and derive an analytical expression for the covariance of $\langle M_{\text{ap}}^3 \rangle$. We test our result by comparing it with the covariance measured in simulated mock data, both simple Gaussian shear fields and full cosmological simulations and investigate the influence of different terms in the covariance by performing mock cosmological analyses.

In our derivation, we will make five crucial findings:

- The covariance consists of six terms, two of which belong to the Gaussian part and four to the non-Gaussian part. These terms all depend on the survey area and window function (Sect. 3.1 and 3.2).
- The individual covariance terms can be estimated from correlation functions of the aperture mass map. These correlation functions need to be known only on scales inside the survey area (Sect. 3.3).
- Under the ‘large-field approximation’, which assumes a broad survey window function, two covariance terms vanish, while the others scale inversely with the survey area. The vanishing terms decrease faster than $1/A$ with survey area A . We refer to them as finite-field terms. One of these terms is already present for Gaussian fields (Sect. 3.4).
- The covariance of $\langle M_{\text{ap}}^3 \rangle$ cannot be obtained from the bispectrum covariance unless the ‘large-field approximation’ is valid. Using a linear transformation of the covariance of a Fourier space quantity to obtain the covariance for a real-space observable has been done for second-order statistics (Joachimi et al. 2021; Friedrich et al. 2021). However, for $\langle M_{\text{ap}}^3 \rangle$ this approach already fails for Gaussian fields if the large-field approximation is not used (Sect. 4).
- Our covariance model, based on an estimator using convergence maps, can be used to obtain upper and lower limits on the covariance for an estimator based on third-order shear correlation functions (Sect. 5.3.2).

This paper is structured as follows. In Sect. 2 we give a short overview of third-order shear statistics, introduce our notation, the third-order aperture mass $\langle M_{\text{ap}}^3 \rangle$ and its estimator. We derive the covariance of this estimator in Sect. 3. In Sect. 4 we show that an alternative derivation of the $\langle M_{\text{ap}}^3 \rangle$ covariance from the bispectrum covariance is not correct. We validate the model by comparing its predictions to simulated data in Sect. 5. Finally, in Sect. 6, we perform mock cosmological analyses to compare the results from the validation data to our model and investigate the impact of the individual covariance terms. We conclude with a summary and discussion in Sect. 7. Throughout this paper, we assume a spatially flat universe. Our covariance modelling code is publically available at <https://github.com/sheydenreich/threepoint/releases>.

2. Theoretical background

In this section, we briefly review some fundamental weak lensing quantities relevant to third-order shear statistics and the covariance calculation in the remainder of this work. We refer to Bartelmann & Schneider (2001); Hoekstra & Jain (2008) or Bartelmann (2010) for in-depth reviews on weak lensing.

One of the fundamental quantities in weak gravitational lensing is the convergence $\kappa(\boldsymbol{\theta})$, which is the normalised surface mass density at angular position $\boldsymbol{\theta}$. In a flat universe, it is related to the density contrast $\delta(\chi\boldsymbol{\theta}, \chi)$ at angular position $\boldsymbol{\theta}$ and comoving distance χ via

$$\kappa(\boldsymbol{\theta}) = \frac{3H_0^2\Omega_m}{2c^2} \int_0^\infty d\chi \, q(\chi) \frac{\delta(\chi\boldsymbol{\theta}, \chi)}{a(\chi)}, \text{ where } q(\chi) = \int_\chi^\infty d\chi' \, p(\chi') \frac{\chi' - \chi}{\chi'}, \quad (1)$$

with the Hubble constant H_0 , the matter density parameter Ω_m , the speed-of-light c , the cosmic scale factor $a(\chi)$ at χ , normalized to unity today, and the probability distribution $p(\chi) d\chi$ of source galaxies in comoving distance.

We treat $\kappa(\boldsymbol{\vartheta})$ as a homogenous and isotropic random field, which is characterised by the full set of its polyspectra \mathcal{P}_n , defined by

$$\langle \tilde{\kappa}(\boldsymbol{\ell}_1) \dots \tilde{\kappa}(\boldsymbol{\ell}_n) \rangle_c = \mathcal{P}_n(\boldsymbol{\ell}_1, \dots, \boldsymbol{\ell}_n) (2\pi)^2 \delta_D(\boldsymbol{\ell}_1 + \dots + \boldsymbol{\ell}_n), \quad (2)$$

where $\tilde{\kappa}(\boldsymbol{\ell})$ is the Fourier transform of κ and the $\langle \dots \rangle_c$ are connected correlation functions. Interesting for us in this work is the powerspectrum P , bispectrum B , trispectrum T , and the pentaspectrum P_6 , defined as

$$P(\ell) = P_2(\boldsymbol{\ell}, -\boldsymbol{\ell}), \quad B(\boldsymbol{\ell}_1, \boldsymbol{\ell}_2) = \mathcal{P}_n(\boldsymbol{\ell}_1, \boldsymbol{\ell}_2, -\boldsymbol{\ell}_1 - \boldsymbol{\ell}_2), \quad T(\boldsymbol{\ell}_1, \boldsymbol{\ell}_2, \boldsymbol{\ell}_3) = \mathcal{P}_n(\boldsymbol{\ell}_1, \boldsymbol{\ell}_2, \boldsymbol{\ell}_3, -\boldsymbol{\ell}_1 - \boldsymbol{\ell}_2 - \boldsymbol{\ell}_3), \quad (3)$$

and

$$P_6(\boldsymbol{\ell}_1, \boldsymbol{\ell}_2, \boldsymbol{\ell}_3, \boldsymbol{\ell}_4, \boldsymbol{\ell}_5) = \mathcal{P}_n(\boldsymbol{\ell}_1, \boldsymbol{\ell}_2, \boldsymbol{\ell}_3, \boldsymbol{\ell}_4, \boldsymbol{\ell}_5, -\boldsymbol{\ell}_1 - \boldsymbol{\ell}_2 - \boldsymbol{\ell}_3 - \boldsymbol{\ell}_4 - \boldsymbol{\ell}_5). \quad (4)$$

The κ -polyspectra are related to the polyspectra $\mathcal{P}_n^{(3d)}$ of the three-dimensional density contrast δ , using the Limber-approximation (Kaiser & Jaffe 1997; Kayo et al. 2013),

$$\mathcal{P}_n(\boldsymbol{\ell}_1, \dots, \boldsymbol{\ell}_n) = \left(\frac{3H_0^2 \Omega_m}{2c^2} \right)^n \int_0^\infty d\chi \frac{q^n(\chi)}{\chi^{n-2} a(\chi)^n} \mathcal{P}_n^{(3d)}(\boldsymbol{\ell}_1/\chi, \dots, \boldsymbol{\ell}_n/\chi, \chi). \quad (5)$$

We model the three-dimensional power spectrum with the revised **Halofit** prescription by Takahashi et al. (2012) and the three-dimensional bispectrum with **BiHalofit** (Takahashi et al. 2020). For the tri- and pentaspectrum, we use the halo model (Cooray & Sheth 2002) with a Sheth–Tormen halo mass function and halo bias (Sheth & Tormen 1999) and Navarro–Frenk–White-halo profiles. To simplify our calculation, we use only the 1-halo term for the trispectrum, which we expect to be dominant at the considered ℓ -scales. For the pentaspectrum, we use the 1- and part of the 2-halo term (see Sect. 3.4 and Appendix C)

The convergence cannot be directly observed, but it is related to the weak lensing shear γ , which describes the change in the observed ellipticity of source galaxies due to the lensing effect. For third-order shear statistics, we are interested in the three-point correlation function of the shear, whose so-called natural components Γ_i were derived by Schneider & Lombardi (2003). However, these components are challenging to handle in practice since they require a large number of bins (typically on the order of 10^3) and are complex to model because they relate to the matter bispectrum via multi-dimensional integrals involving oscillating Bessel functions. As shown in Paper I, more practical quantities with similar information content are the third-order aperture statistics $\langle M_{\text{ap}}^3 \rangle$.

Aperture statistics are moments of the aperture mass M_{ap} ,

$$M_{\text{ap}}(\boldsymbol{\alpha}, \theta) = \int d^2\vartheta U_\theta(|\boldsymbol{\alpha} - \boldsymbol{\vartheta}|) \kappa(\boldsymbol{\vartheta}), \quad \text{with } U_\theta(\vartheta) = \frac{1}{\theta^2} u\left(\frac{\vartheta}{\theta}\right), \quad (6)$$

where U_θ is a filter function with aperture scale radius θ . As long as this filter function is compensated, i.e., $\int d\vartheta \vartheta U_\theta(\vartheta) = 0$, the aperture mass can be estimated from the tangential shear γ_t instead of the convergence (Schneider 1996),

$$M_{\text{ap}}(\boldsymbol{\alpha}, \theta) = \int d^2\vartheta Q_\theta(|\boldsymbol{\alpha} - \boldsymbol{\vartheta}|) \gamma_t(\boldsymbol{\alpha}; \boldsymbol{\vartheta}), \quad \text{with } Q_\theta(\vartheta) = \frac{2}{\vartheta^2} \int_0^\vartheta d\vartheta' \vartheta' U_\theta(\vartheta') - U_\theta(\vartheta). \quad (7)$$

Here, we are interested in the covariance of the third-order aperture statistics $\langle M_{\text{ap}}^3 \rangle$, given by

$$\langle M_{\text{ap}}^3 \rangle(\theta_1, \theta_2, \theta_3) = \langle M_{\text{ap}}(\boldsymbol{\alpha}, \theta_1) M_{\text{ap}}(\boldsymbol{\alpha}, \theta_2) M_{\text{ap}}(\boldsymbol{\alpha}, \theta_3) \rangle, \quad (8)$$

which is our main observable for third-order shear statistics. $\langle M_{\text{ap}}^3 \rangle$ is related to the convergence bispectrum by

$$\langle M_{\text{ap}}^3 \rangle(\theta_1, \theta_2, \theta_3) = \int \frac{d^2\ell_1}{(2\pi)^2} \int \frac{d^2\ell_2}{(2\pi)^2} \tilde{u}(\ell_1 \theta_1) \tilde{u}(\ell_2 \theta_2) \tilde{u}(|\boldsymbol{\ell}_1 + \boldsymbol{\ell}_2| \theta_3) B(\boldsymbol{\ell}_1, \boldsymbol{\ell}_2). \quad (9)$$

For the comparison of the analytical covariance to mock data in Sect. 5 and the estimate of the cosmological parameter analysis in Sect. 6 we choose the exponential filter function from Crittenden et al. (2002),

$$u(x) = \frac{1}{2\pi} \left(1 - \frac{x^2}{2} \right) \exp\left(-\frac{x^2}{2} \right). \quad (10)$$

Based on Eq. (6), $M_{\text{ap}}(\boldsymbol{\alpha}, \theta)$ can be estimated from convergence fields using

$$\hat{M}_{\text{ap}}(\boldsymbol{\alpha}, \theta) = \int_{A'} d^2\vartheta U_\theta(|\boldsymbol{\alpha} - \boldsymbol{\vartheta}|) \kappa(\boldsymbol{\vartheta}), \quad (11)$$

where A' is the full area of the convergence field κ . This estimator can be visualized as placing an aperture of radius θ centred at position $\boldsymbol{\alpha}$ and averaging the convergence values within the aperture weighted by the filter function U_θ (see Fig. 1). The $\langle M_{\text{ap}}^3 \rangle(\theta_1, \theta_2, \theta_3)$ can then be estimated by averaging the product of the $\hat{M}_{\text{ap}}(\boldsymbol{\alpha}, \theta)$ for the three filter radii

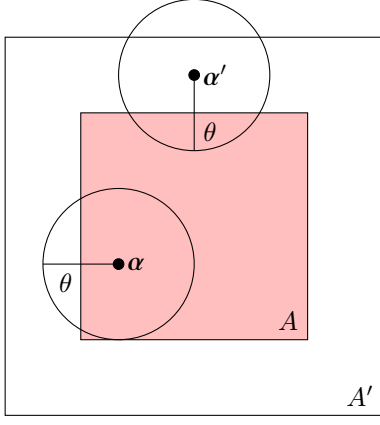


Fig. 1: Illustration of aperture mass estimation. The area A' is the size of the full convergence field, on which we place apertures with scale radius θ , illustrated by the circles, to obtain $M_{\text{ap}}(\alpha, \theta)$. Apertures centred on positions α within the smaller area A lie completely within A' , while apertures centred on positions α' outside of A extend outside of A' , so $M_{\text{ap}}(\alpha', \theta)$ is biased.

over the aperture positions α . However, for α close to the border of the survey area, $\hat{M}_{\text{ap}}(\alpha, \theta)$ is biased because the aperture includes regions outside the survey where κ is not known. Consequently, for an unbiased estimate of $\langle M_{\text{ap}}^3 \rangle$, we only average over an area A smaller than A' , which leads to the estimator

$$\hat{M}_{\text{ap}}^3(\theta_1, \theta_2, \theta_3) = \frac{1}{A} \int_A d^2\alpha \prod_{i=1}^3 \int_{A'} d^2\boldsymbol{\vartheta}_i U_{\theta_i}(|\alpha - \boldsymbol{\vartheta}_i|) \kappa(\boldsymbol{\vartheta}_i). \quad (12)$$

Note that we have assumed here that apertures are placed densely, i.e., that the separation between aperture centres is much smaller than the aperture radius θ , to use a continuous integral over α instead of a sum. If A' is large enough that all U_{θ} centred on points within A vanish outside of A' , we can replace A' with the full \mathbb{R}^2 . We also introduce the survey window function $W_A(\alpha)$, which is unity for α inside A and zero otherwise. With W , we convert integrals over A into integrals over \mathbb{R}^2 , which we denote as two-dimensional integrals without integration borders in the following. The estimator for $\langle M_{\text{ap}}^3 \rangle$ becomes

$$\hat{M}_{\text{ap}}^3(\theta_1, \theta_2, \theta_3) = \frac{1}{A} \int d^2\alpha W_A(\alpha) \left[\prod_{i=1}^3 \int d^2\boldsymbol{\vartheta}_i U_{\theta_i}(|\alpha - \boldsymbol{\vartheta}_i|) \kappa(\boldsymbol{\vartheta}_i) \right]. \quad (13)$$

This estimator is easily applied to simulations, where convergence maps without masks are available (see Sect. 5.2.1). However, this estimator should not be used for survey data that includes masked areas. In that case, one would instead measure the correlation functions Γ_i and convert these into $\langle M_{\text{ap}}^3 \rangle$ (see the discussion in Section 5.3 of Paper I). In this approach, one does not need to decrease the survey area from A' to A because no apertures are laid down. Therefore, the covariance for this estimator is smaller than the covariance for the \hat{M}_{ap}^3 in Eq. (13). However, the unbiased construction of the aperture mass on the whole area A' requires shear estimates outside of A' as well. Therefore, even Γ_i measured from shear estimates on all of A' cannot include the full information that would be contained in an unbiased estimate of \hat{M}_{ap}^3 on A' . Consequently, in the absence of masked regions, we expect the magnitude of the covariance for the estimator based on the Γ_i to be between the covariance for \hat{M}_{ap}^3 for a survey area of A and a survey area of A' . We verify this expectation in Sect. 5.

3. Derivation of aperture statistics covariance from the real-space estimator

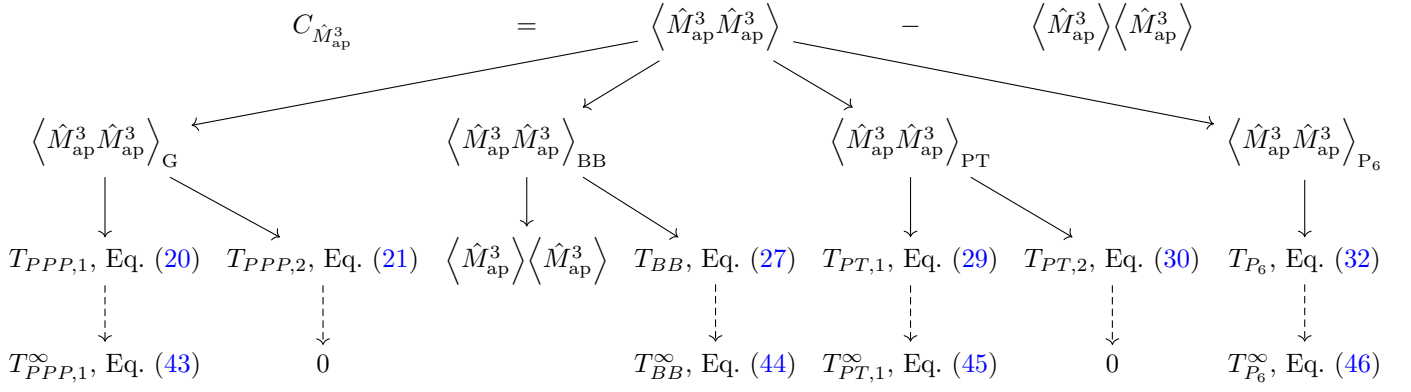
We now derive the covariance $C_{\hat{M}_{\text{ap}}^3}$ of \hat{M}_{ap}^3 . An overview of our calculation is given in Fig. 2, with references to the main equations in our derivation. In the derivation, we find that the covariance comprises several terms, including various permutations of scale radii. For simplicity, we write here "Perm." to indicate permutations; the complete list of permutations for all terms is given in Appendix A. Note that we are not explicitly addressing the effect of shape noise in this section, but that shape noise can be easily included in the derived expressions by replacing the power spectrum P with $P + \sigma_\epsilon^2/2n$, where n is the galaxy number density and σ_ϵ^2 the two-component ellipticity dispersion. We show the validity of this treatment in Appendix B.

The covariance is

$$C_{\hat{M}_{\text{ap}}^3}(\Theta_1, \Theta_2) = \langle \hat{M}_{\text{ap}}^3 \hat{M}_{\text{ap}}^3 \rangle(\Theta_1, \Theta_2) - \langle \hat{M}_{\text{ap}}^3(\Theta_1) \rangle \langle \hat{M}_{\text{ap}}^3(\Theta_2) \rangle, \quad (14)$$

where $\Theta_1 = (\theta_1, \theta_2, \theta_3)$ and $\Theta_2 = (\theta_4, \theta_5, \theta_6)$. With Eq. (13) and $\kappa_i := \kappa(\boldsymbol{\vartheta}_i)$,

$$\begin{aligned} \langle \hat{M}_{\text{ap}}^3 \hat{M}_{\text{ap}}^3 \rangle(\Theta_1, \Theta_2) &= \frac{1}{A^2} \int d^2\alpha_1 \int d^2\alpha_2 W_A(\alpha_1) W_A(\alpha_2) \left[\prod_{i=1}^3 \int d^2\boldsymbol{\vartheta}_i U_{\theta_i}(|\alpha_1 - \boldsymbol{\vartheta}_i|) \right] \left[\prod_{j=4}^6 \int d^2\boldsymbol{\vartheta}_j U_{\theta_j}(|\alpha_2 - \boldsymbol{\vartheta}_j|) \right] \\ &\quad \times \langle \kappa_1 \kappa_2 \kappa_3 \kappa_4 \kappa_5 \kappa_6 \rangle. \end{aligned} \quad (15)$$



————→ Decomposition into summands (see Sect. 3.1 and 3.2)

-----→ Large-field approximation (see Sect. 3.4)

Fig. 2: Schematic representation of the calculation of the covariance $C_{\hat{M}_{\text{ap}}^3}$. The covariance is given by the difference between $\langle \hat{M}_{\text{ap}}^3 \hat{M}_{\text{ap}}^3 \rangle$ and $\langle \hat{M}_{\text{ap}}^3 \rangle \langle \hat{M}_{\text{ap}}^3 \rangle$, the first of which can be decomposed (indicated by solid arrows) into one Gaussian (denoted by G) and three non-Gaussian parts (denoted by BB, PT, and P_6). We discuss the Gaussian part in Sect. 3.1 and the non-Gaussian parts in Sect. 3.2. These parts can be further decomposed into terms depending on different permutations of the aperture scale radii, called $T_{PPP,1}$ to T_{P_6} . For large survey areas, the T_i can be approximated, indicated by dashed arrows, as shown in Sect. 3.4. Under this approximation, two terms vanish, which is why we term them ‘finite-field terms’. Also shown are equation numbers for the relevant expressions.

The six-point correlation can be written in terms of connected correlation functions, denoted by $\langle \rangle_c$. This, together with $\langle \kappa(\boldsymbol{\theta}) \rangle = 0$, leads to

$$\begin{aligned}
 \langle \hat{M}_{\text{ap}}^3 \hat{M}_{\text{ap}}^3 \rangle(\Theta_1, \Theta_2) &= \frac{1}{A^2} \int d^2\alpha_1 \int d^2\alpha_2 W_A(\alpha_1) W_A(\alpha_2) \left[\prod_{i=1}^3 \int d^2\vartheta_i U_{\theta_i}(|\alpha_1 - \boldsymbol{\vartheta}_i|) \right] \left[\prod_{j=4}^6 \int d^2\vartheta_j U_{\theta_j}(|\alpha_2 - \boldsymbol{\vartheta}_j|) \right] \\
 &\times \left[(\langle \kappa_1 \kappa_2 \rangle_c \langle \kappa_3 \kappa_4 \rangle_c \langle \kappa_5 \kappa_6 \rangle_c + 14 \text{ Perm.}) + (\langle \kappa_1 \kappa_2 \kappa_3 \rangle_c \langle \kappa_4 \kappa_5 \kappa_6 \rangle_c + 9 \text{ Perm.}) \right. \\
 &\quad \left. + (\langle \kappa_1 \kappa_2 \rangle_c \langle \kappa_3 \kappa_4 \kappa_5 \kappa_6 \rangle_c + 14 \text{ Perm.}) + \langle \kappa_1 \kappa_2 \kappa_3 \kappa_4 \kappa_5 \kappa_6 \rangle_c \right] \\
 &= \langle \hat{M}_{\text{ap}}^3 \hat{M}_{\text{ap}}^3 \rangle_G(\Theta_1, \Theta_2) + \langle \hat{M}_{\text{ap}}^3 \hat{M}_{\text{ap}}^3 \rangle_{\text{BB}}(\Theta_1, \Theta_2) + \langle \hat{M}_{\text{ap}}^3 \hat{M}_{\text{ap}}^3 \rangle_{\text{PT}}(\Theta_1, \Theta_2) \\
 &\quad + \langle \hat{M}_{\text{ap}}^3 \hat{M}_{\text{ap}}^3 \rangle_{P_6}(\Theta_1, \Theta_2).
 \end{aligned} \tag{16}$$

The first term $\langle \hat{M}_{\text{ap}}^3 \hat{M}_{\text{ap}}^3 \rangle_G$ is the Gaussian part of the covariance – the only part that is non-zero for Gaussian random fields. It depends only on the two-point correlation of κ , or, equivalently, the matter power spectrum $P(\ell)$. The other terms comprise the non-Gaussian part of the covariance. They depend on higher-order polyspectra, namely the bi-, tri- and the pentaspectrum.

3.1. Gaussian part

We first concentrate on the Gaussian part $\langle \hat{M}_{\text{ap}}^3 \hat{M}_{\text{ap}}^3 \rangle_G$, given by

$$\begin{aligned}
 \langle \hat{M}_{\text{ap}}^3 \hat{M}_{\text{ap}}^3 \rangle_G(\Theta_1, \Theta_2) &= \frac{1}{A^2} \int d^2\alpha_1 \int d^2\alpha_2 W_A(\alpha_1) W_A(\alpha_2) \left[\prod_{i=1}^3 \int d^2\vartheta_i U_{\theta_i}(|\alpha_1 - \boldsymbol{\vartheta}_i|) \right] \left[\prod_{j=4}^6 \int d^2\vartheta_j U_{\theta_j}(|\alpha_2 - \boldsymbol{\vartheta}_j|) \right] \\
 &\times [\langle \kappa_1 \kappa_2 \rangle_c \langle \kappa_3 \kappa_4 \rangle_c \langle \kappa_5 \kappa_6 \rangle_c + 14 \text{ Perm.}] .
 \end{aligned} \tag{17}$$

We split the permutations in Eq. (17) into two groups, as

$$\begin{aligned}
\langle \hat{M}_{\text{ap}}^3 \hat{M}_{\text{ap}}^3 \rangle_{\text{G}}(\Theta_1, \Theta_2) &= \frac{1}{A^2} \int d^2\alpha_1 \int d^2\alpha_2 W_A(\alpha_1) W_A(\alpha_2) \left[\prod_{i=1}^3 \int d^2\vartheta_i U_{\theta_i}(|\alpha_1 - \boldsymbol{\vartheta}_i|) \right] \left[\prod_{j=4}^6 \int d^2\vartheta_j U_{\theta_j}(|\alpha_2 - \boldsymbol{\vartheta}_j|) \right] \\
&\quad \times [\langle \kappa_1 \kappa_4 \rangle_c \langle \kappa_3 \kappa_5 \rangle_c \langle \kappa_2 \kappa_6 \rangle_c + 5 \text{ Perm.}] \\
&+ \frac{1}{A^2} \int d^2\alpha_1 \int d^2\alpha_2 W_A(\alpha_1) W_A(\alpha_2) \left[\prod_{i=1}^3 \int d^2\vartheta_i U_{\theta_i}(|\alpha_1 - \boldsymbol{\vartheta}_i|) \right] \left[\prod_{j=4}^6 \int d^2\vartheta_j U_{\theta_j}(|\alpha_2 - \boldsymbol{\vartheta}_j|) \right] \\
&\quad \times [\langle \kappa_1 \kappa_2 \rangle_c \langle \kappa_3 \kappa_4 \rangle_c \langle \kappa_5 \kappa_6 \rangle_c + 8 \text{ Perm.}] \\
&= T_{PPP,1}(\Theta_1, \Theta_2) + T_{PPP,2}(\Theta_1, \Theta_2) .
\end{aligned} \tag{18}$$

The first group consists of six terms, in which for all three $\langle \kappa_i \kappa_j \rangle_c$, the first index $i \in \{1, 2, 3\}$, and the second index $j \in \{4, 5, 6\}$. The second group consists of the nine other permutations. To evaluate $T_{PPP,1}$ and $T_{PPP,2}$, we use Eq. (2) for $n = 2$ and

$$\int d^2\vartheta U_{\theta}(|\alpha - \boldsymbol{\vartheta}|) e^{-i\boldsymbol{\ell} \cdot \boldsymbol{\vartheta}} = \tilde{u}(\ell\theta) e^{-i\boldsymbol{\ell} \cdot \boldsymbol{\alpha}} , \tag{19}$$

and find

$$\begin{aligned}
T_{PPP,1}(\Theta_1, \Theta_2) &= \frac{1}{A^2} \left[\prod_{i=1}^3 \int \frac{d^2\ell_i}{(2\pi)^2} P(\ell_i) \right] [\tilde{u}(\ell_1\theta_1) \tilde{u}(\ell_2\theta_2) \tilde{u}(\ell_3\theta_3) \tilde{u}(\ell_1\theta_4) \tilde{u}(\ell_2\theta_5) \tilde{u}(\ell_3\theta_6) + 5 \text{ Perm.}] \\
&\quad \times \int d^2\alpha_1 \int d^2\alpha_2 W_A(\alpha_1) W_A(\alpha_2) e^{-i(\alpha_1 - \alpha_2) \cdot (\boldsymbol{\ell}_1 + \boldsymbol{\ell}_2 + \boldsymbol{\ell}_3)} \\
&= \left[\prod_{i=1}^3 \int \frac{d^2\ell_i}{(2\pi)^2} P(\ell_i) \right] G_A(\boldsymbol{\ell}_1 + \boldsymbol{\ell}_2 + \boldsymbol{\ell}_3) [\tilde{u}(\ell_1\theta_1) \tilde{u}(\ell_2\theta_2) \tilde{u}(\ell_3\theta_3) \tilde{u}(\ell_1\theta_4) \tilde{u}(\ell_2\theta_5) \tilde{u}(\ell_3\theta_6) + 5 \text{ Perm.}] ,
\end{aligned} \tag{20}$$

and

$$\begin{aligned}
T_{PPP,2}(\Theta_1, \Theta_2) &= \frac{1}{A^2} \left[\prod_{i=1}^3 \int \frac{d^2\ell_i}{(2\pi)^2} P(\ell_i) \right] [\tilde{u}(\ell_1\theta_1) \tilde{u}(\ell_1\theta_2) \tilde{u}(\ell_2\theta_3) \tilde{u}(\ell_2\theta_4) \tilde{u}(\ell_3\theta_5) \tilde{u}(\ell_3\theta_6) + 8 \text{ Perm.}] \\
&\quad \times \int d^2\alpha_1 \int d^2\alpha_2 W_A(\alpha_1) W_A(\alpha_2) e^{-i(\alpha_1 - \alpha_2) \cdot \boldsymbol{\ell}_2} \\
&= \left[\prod_{i=1}^3 \int \frac{d^2\ell_i}{(2\pi)^2} P(\ell_i) \right] G_A(\boldsymbol{\ell}_2) [\tilde{u}(\ell_1\theta_1) \tilde{u}(\ell_1\theta_2) \tilde{u}(\ell_2\theta_3) \tilde{u}(\ell_2\theta_4) \tilde{u}(\ell_3\theta_5) \tilde{u}(\ell_3\theta_6) + 8 \text{ Perm.}] ,
\end{aligned} \tag{21}$$

where the geometry factor $G_A(\boldsymbol{\ell})$, defined by

$$G_A(\boldsymbol{\ell}) = \frac{1}{A^2} \int d^2\alpha_1 \int d^2\alpha_2 W_A(\alpha_1) W_A(\alpha_2) e^{-i(\boldsymbol{\alpha}_1 - \boldsymbol{\alpha}_2) \cdot \boldsymbol{\ell}} , \tag{22}$$

contains the full dependence of the covariance on the survey area and geometry. For a square survey with side length $\vartheta_{\text{max}} = \sqrt{A}$, and $\boldsymbol{\ell} = (\ell_x, \ell_y)$ the factor is

$$G_{A,\text{square}}(\boldsymbol{\ell}) = \frac{4 \sin^2(\ell_x \vartheta_{\text{max}}/2)}{\ell_x^2 \vartheta_{\text{max}}^2} \frac{4 \sin^2(\ell_y \vartheta_{\text{max}}/2)}{\ell_y^2 \vartheta_{\text{max}}^2} . \tag{23}$$

The geometry factor G_A is related to a function $E_A(\boldsymbol{\eta})$, which, for a point $\boldsymbol{\alpha}$ within A , gives the probability for a second point at $\boldsymbol{\alpha} + \boldsymbol{\eta}$ to lie within A as well. It is given by

$$E_A(\boldsymbol{\eta}) = \frac{1}{A} \int d^2\alpha W_A(\alpha) W_A(\alpha + \boldsymbol{\eta}) , \quad \text{so that} \quad G_A(\boldsymbol{\ell}) = \frac{1}{A} \int_A d^2\eta E_A(\boldsymbol{\eta}) e^{-i\boldsymbol{\eta} \cdot \boldsymbol{\ell}} . \tag{24}$$

For a square area, $E_A(\boldsymbol{\eta})$ was determined by [Heydenreich et al. \(2020\)](#). It is unity for vanishing separation $|\boldsymbol{\eta}| = 0$ and smoothly declines to zero for $\boldsymbol{\eta}$ outside the square.

3.2. Non-Gaussian part

We now derive the non-Gaussian part of the covariance. First, we calculate the covariance part $\langle \hat{M}_{\text{ap}}^3 \hat{M}_{\text{ap}}^3 \rangle_{BB}$, which depends on third-order correlations of κ . We divide this term into two parts, as

$$\begin{aligned} \langle \hat{M}_{\text{ap}}^3 \hat{M}_{\text{ap}}^3 \rangle_{BB}(\Theta_1, \Theta_2) &= \frac{1}{A^2} \int d^2\alpha_1 \int d^2\alpha_2 \left[\prod_{i=1}^3 \int d^2\vartheta_i U_{\theta_i}(|\alpha_1 - \boldsymbol{\vartheta}_i|) \right] \left[\prod_{j=4}^6 \int d^2\vartheta_j U_{\theta_j}(|\alpha_2 - \boldsymbol{\vartheta}_j|) \right] \\ &\quad \times W_A(\alpha_1) W_A(\alpha_2) \{ \langle \kappa_1 \kappa_2 \kappa_3 \rangle_c \langle \kappa_4 \kappa_5 \kappa_6 \rangle_c + [\langle \kappa_4 \kappa_2 \kappa_3 \rangle_c \langle \kappa_1 \kappa_5 \kappa_6 \rangle_c + 8 \text{ Perm.}] \} \\ &= \langle \hat{M}_{\text{ap}}^3(\theta_1, \theta_2, \theta_3) \rangle \langle \hat{M}_{\text{ap}}^3(\theta_4, \theta_5, \theta_6) \rangle + T_{BB}(\Theta_1, \Theta_2). \end{aligned} \quad (25)$$

The first term cancels with the second term in the definition of the covariance of the estimator in Eq. (14). The term T_{BB} is

$$\begin{aligned} T_{BB}(\Theta_1, \Theta_2) &= \frac{1}{A^2} \int d^2\alpha_1 \int d^2\alpha_2 \left[\prod_{i=1}^3 \int d^2\vartheta_i U_{\theta_i}(|\alpha_1 - \boldsymbol{\vartheta}_i|) \right] \left[\prod_{j=4}^6 \int d^2\vartheta_j U_{\theta_j}(|\alpha_2 - \boldsymbol{\vartheta}_j|) \right] W_A(\alpha_1) W_A(\alpha_2) \\ &\quad \times [\langle \kappa_4 \kappa_2 \kappa_3 \rangle_c \langle \kappa_1 \kappa_5 \kappa_6 \rangle_c + 8 \text{ Perm.}] . \end{aligned} \quad (26)$$

Using Eq. (2) for $n = 3$ to introduce the bispectrum and the definition of G_A in Eq. (22) leads to

$$\begin{aligned} T_{BB}(\Theta_1, \Theta_2) &= \int \frac{d^2\ell_1}{(2\pi)^2} \int \frac{d^2\ell_2}{(2\pi)^2} \int \frac{d^2\ell_4}{(2\pi)^2} \int \frac{d^2\ell_5}{(2\pi)^2} B(\boldsymbol{\ell}_1, \boldsymbol{\ell}_2) B(\boldsymbol{\ell}_4, \boldsymbol{\ell}_5) G_A(\boldsymbol{\ell}_1 - \boldsymbol{\ell}_4) \\ &\quad \times [\tilde{u}(\ell_4 \theta_1) \tilde{u}(\ell_2 \theta_2) \tilde{u}(|\boldsymbol{\ell}_1 + \boldsymbol{\ell}_2| \theta_3) \tilde{u}(\ell_1 \theta_4) \tilde{u}(\ell_5 \theta_5) \tilde{u}(|\boldsymbol{\ell}_4 + \boldsymbol{\ell}_5| \theta_6) + 8 \text{ Perm.}] . \end{aligned} \quad (27)$$

Second, we calculate the covariance part $\langle \hat{M}_{\text{ap}}^3 \hat{M}_{\text{ap}}^3 \rangle_{PT}$. We divide this term into two parts as

$$\begin{aligned} \langle \hat{M}_{\text{ap}}^3 \hat{M}_{\text{ap}}^3 \rangle_{PT}(\Theta_1, \Theta_2) &= \frac{1}{A^2} \int d^2\alpha_1 \int d^2\alpha_2 \left[\prod_{i=1}^3 \int d^2\vartheta_i U_{\theta_i}(|\alpha_1 - \boldsymbol{\vartheta}_i|) \right] \left[\prod_{j=4}^6 \int d^2\vartheta_j U_{\theta_j}(|\alpha_2 - \boldsymbol{\vartheta}_j|) \right] \\ &\quad \times W_A(\alpha_1) W_A(\alpha_2) [\langle \kappa_1 \kappa_4 \rangle_c \langle \kappa_2 \kappa_3 \kappa_5 \kappa_6 \rangle_c + 8 \text{ Perm.} + \langle \kappa_1 \kappa_2 \rangle_c \langle \kappa_3 \kappa_4 \kappa_5 \kappa_6 \rangle_c + 5 \text{ Perm.}] \\ &= T_{PT,1}(\Theta_1, \Theta_2) + T_{PT,2}(\Theta_1, \Theta_2). \end{aligned} \quad (28)$$

Here, the first permutations contain all terms where the two-point correlation $\langle \kappa_i \kappa_j \rangle$ has $i \in \{1, 2, 3\}$ and $j \in \{4, 5, 6\}$. The second permutations contain all other terms. We introduce the power- and trispectrum with Eq. (2), and find

$$\begin{aligned} T_{PT,1}(\Theta_1, \Theta_2) &= \int \frac{d^2\ell_1}{(2\pi)^2} \int \frac{d^2\ell_2}{(2\pi)^2} \int \frac{d^2\ell_3}{(2\pi)^2} \int \frac{d^2\ell_4}{(2\pi)^2} P(\ell_1) T(\boldsymbol{\ell}_2, \boldsymbol{\ell}_3, \boldsymbol{\ell}_4) G_A(\boldsymbol{\ell}_1 + \boldsymbol{\ell}_2 + \boldsymbol{\ell}_3) \\ &\quad \times [\tilde{u}(\ell_1 \theta_1) \tilde{u}(\ell_2 \theta_2) \tilde{u}(\ell_3 \theta_3) \tilde{u}(\ell_1 \theta_4) \tilde{u}(\ell_4 \theta_5) \tilde{u}(|\boldsymbol{\ell}_2 + \boldsymbol{\ell}_3 + \boldsymbol{\ell}_4| \theta_6) + 8 \text{ Perm.}] , \end{aligned} \quad (29)$$

and

$$\begin{aligned} T_{PT,2}(\Theta_1, \Theta_2) &= \int \frac{d^2\ell_1}{(2\pi)^2} \int \frac{d^2\ell_2}{(2\pi)^2} \int \frac{d^2\ell_3}{(2\pi)^2} \int \frac{d^2\ell_4}{(2\pi)^2} P(\ell_1) T(\boldsymbol{\ell}_2, \boldsymbol{\ell}_3, \boldsymbol{\ell}_4) G_A(\boldsymbol{\ell}_2) \\ &\quad \times [\tilde{u}(\ell_1 \theta_1) \tilde{u}(\ell_1 \theta_2) \tilde{u}(\ell_2 \theta_3) \tilde{u}(\ell_3 \theta_4) \tilde{u}(\ell_4 \theta_5) \tilde{u}(|\boldsymbol{\ell}_2 + \boldsymbol{\ell}_3 + \boldsymbol{\ell}_4| \theta_6) + 5 \text{ Perm.}] . \end{aligned} \quad (30)$$

Finally, we consider $\langle \hat{M}_{\text{ap}}^3 \hat{M}_{\text{ap}}^3 \rangle_{P_6}$, which is

$$\begin{aligned} \langle \hat{M}_{\text{ap}}^3 \hat{M}_{\text{ap}}^3 \rangle_{P_6}(\Theta_1, \Theta_2) &= \frac{1}{A^2} \int d^2\alpha_1 \int d^2\alpha_2 W_A(\alpha_1) W_A(\alpha_2) \\ &\quad \times \left[\prod_{i=1}^3 \int d^2\vartheta_i U_{\theta_i}(|\alpha_1 - \boldsymbol{\vartheta}_i|) \right] \left[\prod_{j=4}^6 \int d^2\vartheta_j U_{\theta_j}(|\alpha_2 - \boldsymbol{\vartheta}_j|) \right] \langle \kappa_1 \kappa_2 \kappa_3 \kappa_4 \kappa_5 \kappa_6 \rangle_c \\ &= T_{P_6}(\Theta_1, \Theta_2). \end{aligned} \quad (31)$$

The term T_{P_6} is, with Eq. (2) for $n = 6$,

$$\begin{aligned} T_{P_6}(\Theta_1, \Theta_2) &= \int \frac{d^2\ell_1}{(2\pi)^2} \int \frac{d^2\ell_2}{(2\pi)^2} \int \frac{d^2\ell_3}{(2\pi)^2} \int \frac{d^2\ell_4}{(2\pi)^2} \int \frac{d^2\ell_5}{(2\pi)^2} P_6(\boldsymbol{\ell}_1, \boldsymbol{\ell}_2, \boldsymbol{\ell}_3, \boldsymbol{\ell}_4, \boldsymbol{\ell}_5) G_A(\boldsymbol{\ell}_1 + \boldsymbol{\ell}_2 + \boldsymbol{\ell}_3) \\ &\quad \times \tilde{u}(\ell_1 \theta_1) \tilde{u}(\ell_2 \theta_2) \tilde{u}(\ell_3 \theta_3) \tilde{u}(\ell_4 \theta_4) \tilde{u}(\ell_5 \theta_5) \tilde{u}(|\boldsymbol{\ell}_1 + \boldsymbol{\ell}_2 + \boldsymbol{\ell}_3 + \boldsymbol{\ell}_4 + \boldsymbol{\ell}_5| \theta_6) . \end{aligned} \quad (32)$$

3.3. Connection of covariance terms to aperture mass correlation functions

We now show that the individual covariance terms are related to correlation functions of the aperture mass. While this might appear like a meaningless algebraic exercise, it has an important corollary: Since the correlation functions can be measured, we can estimate all individual terms of the covariance in the validation data. Thereby, the analytic expressions can be validated.

We define the n -th order aperture mass correlation functions $M_{\text{ap}}^{n,m}$, as

$$M_{\text{ap}}^{n,m}(\theta_1, \dots, \theta_m; \theta_{m+1}, \dots, \theta_n; \boldsymbol{\eta}) = \langle M_{\text{ap}}(\boldsymbol{\vartheta}, \theta_1) \dots M_{\text{ap}}(\boldsymbol{\vartheta}, \theta_m) M_{\text{ap}}(\boldsymbol{\vartheta} + \boldsymbol{\eta}, \theta_{m+1}) M_{\text{ap}}(\boldsymbol{\vartheta} + \boldsymbol{\eta}, \theta_n) \rangle . \quad (33)$$

Note that this function is symmetric in its first m aperture radii and in its second $n - m$ aperture radii. The correlation functions can be expressed in terms of the convergence as

$$M_{\text{ap}}^{n,m}(\theta_1, \dots, \theta_m; \theta_{m+1}, \dots, \theta_n; \boldsymbol{\eta}) = \left[\prod_{i=1}^m \int d^2\vartheta_i U_{\theta_i}(\vartheta_i) \right] \left[\prod_{j=m+1}^n \int d^2\vartheta_j U_{\theta_j}(|\boldsymbol{\vartheta}_j + \boldsymbol{\eta}|) \right] \langle \kappa_1 \dots \kappa_n \rangle , \quad (34)$$

where $\kappa_i = \kappa(\boldsymbol{\vartheta}_i)$ and the average over the convergence contains both connected and unconnected terms. Using $n = 2$, Eq. (18) and the definition of $E(\boldsymbol{\eta})$ from Eq. (24), the first Gaussian covariance term can be written as

$$\begin{aligned} T_{PPP,1}(\Theta_1, \Theta_2) &= \frac{1}{A^2} \int d^2\alpha_1 \int d^2\alpha_2 W_A(\alpha_1) W_A(\alpha_2) M_{\text{ap}}^{2,1}(\theta_1; \theta_4; |\alpha_1 - \alpha_2|) M_{\text{ap}}^{2,1}(\theta_2; \theta_5; |\alpha_1 - \alpha_2|) \\ &\quad \times M_{\text{ap}}^{2,1}(\theta_3; \theta_6; |\alpha_1 - \alpha_2|) + 5 \text{ Perm.} \\ &= \frac{1}{A} \int_A d^2\eta E_A(\boldsymbol{\eta}) M_{\text{ap}}^{2,1}(\theta_1; \theta_4; \boldsymbol{\eta}) M_{\text{ap}}^{2,1}(\theta_2; \theta_5; \boldsymbol{\eta}) M_{\text{ap}}^{2,1}(\theta_3; \theta_6; \boldsymbol{\eta}) + 5 \text{ Perm.} . \end{aligned} \quad (35)$$

Similarly, $T_{PPP,2}$ can be written as

$$T_{PPP,2}(\Theta_1, \Theta_2) = M_{\text{ap}}^2(\theta_1, \theta_2) M_{\text{ap}}^2(\theta_5, \theta_6) \frac{1}{A} \int_A d^2\eta E_A(\boldsymbol{\eta}) M_{\text{ap}}^{2,1}(\theta_3; \theta_4; \boldsymbol{\eta}) + 8 \text{ Perm.} , \quad (36)$$

where $M_{\text{ap}}^2(\theta_1, \theta_2) = M_{\text{ap}}^{2,0}(\theta_1, \theta_2, \eta = 0)$ is the second-order aperture statistic.

The term T_{BB} becomes

$$T_{BB}(\Theta_1, \Theta_2) = \frac{1}{A} \int_A d^2\eta E_A(\boldsymbol{\eta}) M_{\text{ap}}^{3,2}(\theta_1, \theta_2; \theta_4; \boldsymbol{\eta}) M_{\text{ap}}^{3,2}(\theta_5, \theta_6; \theta_3; \boldsymbol{\eta}) + 8 \text{ Perm.} . \quad (37)$$

We relate $T_{PT,1}$ and $T_{PT,2}$ to the correlation functions $M_{\text{ap}}^{4,3}$ and $M_{\text{ap}}^{4,2}$. We stress that these correlation functions depend on both connected and unconnected correlations of the convergence field. Using Eq. (28), we find

$$T_{PT,1}(\Theta_1, \Theta_2) = \frac{1}{A} \int_A d^2\eta E_A(\boldsymbol{\eta}) M_{\text{ap}}^{2,1}(\theta_1; \theta_4; \boldsymbol{\eta}) M_{\text{ap}}^{4,2}(\theta_2, \theta_3; \theta_5, \theta_6; \boldsymbol{\eta}) + 8 \text{ Perm.} - [3T_{PPP,1}(\Theta_1, \Theta_2) + T_{PPP,2}(\Theta_1, \Theta_2)] , \quad (38)$$

and

$$T_{PT,2}(\Theta_1, \Theta_2) = M_{\text{ap}}^2(\theta_1, \theta_2) \frac{1}{A} \int_A d^2\eta E_A(\boldsymbol{\eta}) M_{\text{ap}}^{4,3}(\theta_4, \theta_5, \theta_6; \theta_3; \boldsymbol{\eta}) + 5 \text{ Perm.} - [2T_{PPP,2}(\Theta_1, \Theta_2)] , \quad (39)$$

where the square brackets denote the terms caused by unconnected terms in $M_{\text{ap}}^{4,3}$ and $M_{\text{ap}}^{4,2}$. The term T_{P_6} cannot be obtained from the aperture mass correlation functions independently of the other covariance terms. However, using Eq. (15), the full covariance $C_{\dot{M}_{\text{ap}}^3}$ is

$$C_{\dot{M}_{\text{ap}}^3}(\Theta_1, \Theta_2) = \frac{1}{A} \int_A d^2\eta E_A(\boldsymbol{\eta}) M_{\text{ap}}^{6,3}(\theta_1, \theta_2, \theta_3; \theta_4, \theta_5, \theta_6; \boldsymbol{\eta}) , \quad (40)$$

so T_{P_6} can be estimated with

$$T_{P_6}(\Theta_1, \Theta_2) = C_{\dot{M}_{\text{ap}}^3}(\Theta_1, \Theta_2) - T_{PPP,1}(\Theta_1, \Theta_2) - T_{PPP,2}(\Theta_1, \Theta_2) - T_{BB}(\Theta_1, \Theta_2) - T_{PT,1}(\Theta_1, \Theta_2) - T_{PT,2}(\Theta_1, \Theta_2) . \quad (41)$$

3.4. Large-field approximation

In the previous sections, we have derived six components for the covariance, which might appear analogous to each other. However, we will show here that the terms $T_{PPP,2}$ and $T_{PT,2}$ show significantly different behaviour with survey size than the other terms. For this, we consider the case of a large survey area, for which the window function W_A can be approximated as one everywhere. In this case, the geometry factor G_A becomes

$$G_A(\boldsymbol{\ell}) \rightarrow \frac{(2\pi)^2}{A} \delta_D(\boldsymbol{\ell}) . \quad (42)$$

In this approximation, the terms $T_{PPP,1}$, T_{BB} , $T_{PT,1}$ and T_{P_6} become

$$T_{PPP,1}^\infty(\Theta_1, \Theta_2) = \frac{1}{A} \int \frac{d^2\ell_1}{(2\pi)^2} \int \frac{d^2\ell_2}{(2\pi)^2} P(\ell_1) P(\ell_2) P(|\boldsymbol{\ell}_1 + \boldsymbol{\ell}_2|) \times [\tilde{u}(\ell_1 \theta_1) \tilde{u}(\ell_2 \theta_2) \tilde{u}(|\boldsymbol{\ell}_1 + \boldsymbol{\ell}_2| \theta_3) \tilde{u}(\ell_1 \theta_4) \tilde{u}(\ell_2 \theta_5) \tilde{u}(|\boldsymbol{\ell}_1 + \boldsymbol{\ell}_2| \theta_6) + 5 \text{ Perm.}] , \quad (43)$$

$$T_{BB}^\infty(\Theta_1, \Theta_2) = \frac{1}{A} \int \frac{d^2\ell_1}{(2\pi)^2} \int \frac{d^2\ell_2}{(2\pi)^2} \int \frac{d^2\ell_3}{(2\pi)^2} B(\boldsymbol{\ell}_1, \boldsymbol{\ell}_2) B(\boldsymbol{\ell}_1, \boldsymbol{\ell}_3) \times [\tilde{u}(\ell_1 \theta_1) \tilde{u}(\ell_2 \theta_2) \tilde{u}(|\boldsymbol{\ell}_1 + \boldsymbol{\ell}_2| \theta_3) \tilde{u}(\ell_1 \theta_4) \tilde{u}(\ell_3 \theta_5) \tilde{u}(|\boldsymbol{\ell}_1 + \boldsymbol{\ell}_3| \theta_6) + 8 \text{ Perm.}] , \quad (44)$$

$$T_{PT,1}^\infty(\Theta_1, \Theta_2) = \frac{1}{A} \int \frac{d^2\ell_1}{(2\pi)^2} \int \frac{d^2\ell_2}{(2\pi)^2} \int \frac{d^2\ell_3}{(2\pi)^2} P(\ell_1) T(\ell_2, -\boldsymbol{\ell}_1 - \boldsymbol{\ell}_2, \ell_3) \times [\tilde{u}(\ell_1 \theta_1) \tilde{u}(\ell_2 \theta_2) \tilde{u}(|\boldsymbol{\ell}_1 + \boldsymbol{\ell}_2| \theta_3) \tilde{u}(\ell_1 \theta_4) \tilde{u}(\ell_3 \theta_5) \tilde{u}(|\boldsymbol{\ell}_3 - \boldsymbol{\ell}_1| \theta_6) + 8 \text{ Perm.}] , \quad (45)$$

and

$$T_{P_6}^\infty(\Theta_1, \Theta_2) = \frac{1}{A} \int \frac{d^2\ell_1}{(2\pi)^2} \int \frac{d^2\ell_2}{(2\pi)^2} \int \frac{d^2\ell_3}{(2\pi)^2} \int \frac{d^2\ell_4}{(2\pi)^2} P_6(\boldsymbol{\ell}_1, \boldsymbol{\ell}_2, -\boldsymbol{\ell}_1 - \boldsymbol{\ell}_2, \boldsymbol{\ell}_3, \boldsymbol{\ell}_4) \times \tilde{u}(\ell_1 \theta_1) \tilde{u}(\ell_2 \theta_2) \tilde{u}(|\boldsymbol{\ell}_1 + \boldsymbol{\ell}_2| \theta_3) \tilde{u}(\ell_3 \theta_4) \tilde{u}(\ell_4 \theta_5) \tilde{u}(|\boldsymbol{\ell}_3 + \boldsymbol{\ell}_4| \theta_6) . \quad (46)$$

These terms scale with the inverse survey area, as is commonly expected for covariance. The terms $T_{PPP,2}$ and $T_{PT,2}$, though, behave differently. Applying the approximation leads to

$$T_{PPP,2}^\infty(\Theta_1, \Theta_2) = \frac{1}{A} \int \frac{d^2\ell_1}{(2\pi)^2} \int \frac{d^2\ell_3}{(2\pi)^2} P(\ell_1) P(0) P(\ell_3) [\tilde{u}(\ell_1 \theta_1) \tilde{u}(\ell_1 \theta_2) \tilde{u}(0) \tilde{u}(0) \tilde{u}(\ell_3 \theta_5) \tilde{u}(\ell_3 \theta_6) + 8 \text{ Perm.}] = 0 , \quad (47)$$

and

$$T_{PT,2}^\infty(\Theta_1, \Theta_2) = \frac{1}{A} \int \frac{d^2\ell_1}{(2\pi)^2} \int \frac{d^2\ell_2}{(2\pi)^2} \int \frac{d^2\ell_3}{(2\pi)^2} P(\ell_1) T(0, \boldsymbol{\ell}_2, \boldsymbol{\ell}_3) [\tilde{u}(\ell_1 \theta_1) \tilde{u}(\ell_1 \theta_2) \times \tilde{u}(0) \tilde{u}(\ell_2 \theta_4) \tilde{u}(\ell_3 \theta_5) \tilde{u}(|\boldsymbol{\ell}_2 + \boldsymbol{\ell}_3| \theta_6) + 5 \text{ Perm.}] = 0 . \quad (48)$$

Both terms vanish because the filter function $\tilde{u}(0) = 0$ for a compensated filter. The same can be observed when writing $T_{PPP,2}$ in terms of the aperture mass correlation function (Eqs. 36). The large-field approximation implies $E(\boldsymbol{\eta}) = 1$, so for a square survey with sidelength ϑ_{\max}

$$T_{PPP,2}^\infty(\Theta_1, \Theta_2) = M_{\text{ap}}^2(\theta_1, \theta_2) M_{\text{ap}}^2(\theta_5, \theta_6) \frac{1}{A} \int_A d^2\eta M_{\text{ap}}^{2,1}(\theta_3; \theta_4; \boldsymbol{\eta}) + 8 \text{ Perm.} , \quad (49)$$

Since $M_{\text{ap}}^{2,1}$ is a correlation function of a quantity with vanishing mean, the integral over $\boldsymbol{\eta}$ vanishes as $A \rightarrow \mathbb{R}^2$ and $T_{PPP,2}$ declines to zero faster than $1/A$. The same argument can be made for $T_{PT,2}$, which depends on the integral of the correlation function $M_{\text{ap}}^{4,3}$. Consequently, these terms are directly connected to the finiteness of the survey area, which is why we will refer to them as ‘finite-field terms’ of the covariance.

As shown in Eq. (23), the geometry factor G_A is typically a strongly oscillating function. Consequently, integrals over this function are difficult to evaluate numerically. Therefore, in the following, we use the approximations $T_{PPP,1}^\infty$, T_{BB}^∞ and $T_{PT,1}^\infty$ unless otherwise noted. However, as we will show in Sect. 6 using $T_{P_6}^\infty$ instead of T_{P_6} neglects a significant part of the covariance. As shown in Appendix C, T_{P_6} can be approximated as

$$T_{P_6}(\Theta_1, \Theta_2) \simeq T_{P_6}^\infty(\Theta_1, \Theta_2) + T_{P_6,2h}(\Theta_1, \Theta_2) , \quad (50)$$

with $T_{P_6,2h}$ given by Eq. (C.7). The term $T_{P_6,2h}$ is similar to the finite-field terms $T_{PPP,2}$ and $T_{PT,2}$ since it does not scale inversely with survey area and vanishes under the large-field approximation.

The approximations $T_{PPP,1}^\infty$, T_{BB}^∞ , and $T_{PT,1}^\infty$ also neglect part of the covariance. However, since these terms are sub-dominant for the total covariance, as we will show in Sect. 5, we deem the approximation appropriate for these terms.

4. Attempt at alternative derivation of Gaussian \hat{M}_{ap}^3 covariance from bispectrum covariance

An alternative approach to finding an analytic covariance estimate of a real-space observable is via the covariance of the corresponding Fourier space quantity. As the $\langle M_{\text{ap}}^3 \rangle$ are related to the bispectrum B via Eq. (9), it might appear natural to derive the covariance of $\langle M_{\text{ap}}^3 \rangle$ from the covariance of B . However, this is impossible for finite survey areas without using the large-field approximation, even for Gaussian fields. To see this, we rewrite Eq. (9) as

$$\langle M_{\text{ap}}^3 \rangle(\theta_1, \theta_2, \theta_3) = (2\pi)^2 \left[\prod_{i=1}^3 \int \frac{d^2 \ell_i}{(2\pi)^2} \tilde{u}(\ell_i \theta_i) \right] \mathcal{P}_3(\boldsymbol{\ell}_1, \boldsymbol{\ell}_2, \boldsymbol{\ell}_3) \delta_{\text{D}}(\boldsymbol{\ell}_1 + \boldsymbol{\ell}_2 + \boldsymbol{\ell}_3), \quad (51)$$

where we remind that $\mathcal{P}_3(\boldsymbol{\ell}_1, \boldsymbol{\ell}_2, \boldsymbol{\ell}_3) = B(\boldsymbol{\ell}_1, \boldsymbol{\ell}_2)$. One could then assume that the covariance $C_{\langle M_{\text{ap}}^3 \rangle}$ were given by

$$C_{\hat{M}_{\text{ap}}^3}(\Theta_1, \Theta_2) = (2\pi)^4 \left[\prod_{i=1}^6 \int \frac{d^2 \ell_i}{(2\pi)^2} \tilde{u}(\ell_i \theta_i) \right] C_B(\boldsymbol{\ell}_1, \boldsymbol{\ell}_2, \boldsymbol{\ell}_3, \boldsymbol{\ell}_4, \boldsymbol{\ell}_5, \boldsymbol{\ell}_6) \delta_{\text{D}}(\boldsymbol{\ell}_1 + \boldsymbol{\ell}_2 + \boldsymbol{\ell}_3) \delta_{\text{D}}(\boldsymbol{\ell}_4 + \boldsymbol{\ell}_5 + \boldsymbol{\ell}_6), \quad (52)$$

where C_B is the covariance of the bispectrum. Then, it should be possible to infer C_B from $C_{\hat{M}_{\text{ap}}^3}$. However, the Gaussian part of $C_{\hat{M}_{\text{ap}}^3}$ is

$$\begin{aligned} T_{PPP,1}(\Theta_1, \Theta_2) + T_{PPP,2}(\Theta_1, \Theta_2) &= (2\pi)^6 \left[\prod_{i=1}^6 \int \frac{d^2 \ell_i}{(2\pi)^2} \tilde{u}(\ell_i \theta_i) \right] P(\ell_1) P(\ell_2) P(\ell_3) \\ &\times \left\{ [G_A(\boldsymbol{\ell}_1 + \boldsymbol{\ell}_2 + \boldsymbol{\ell}_3) \delta_{\text{D}}(\boldsymbol{\ell}_1 + \boldsymbol{\ell}_4) \delta_{\text{D}}(\boldsymbol{\ell}_2 + \boldsymbol{\ell}_5) \delta_{\text{D}}(\boldsymbol{\ell}_3 + \boldsymbol{\ell}_6) + 5 \text{ Perm.}] \right. \\ &\left. + [G_A(\boldsymbol{\ell}_2) \delta_{\text{D}}(\boldsymbol{\ell}_1 + \boldsymbol{\ell}_2) \delta_{\text{D}}(\boldsymbol{\ell}_3 + \boldsymbol{\ell}_4) \delta_{\text{D}}(\boldsymbol{\ell}_5 + \boldsymbol{\ell}_6) + 8 \text{ Perm.}] \right\}. \end{aligned} \quad (53)$$

For Eq. (52) to hold true, we need the expression in braces to equal $f(\boldsymbol{\ell}_1, \boldsymbol{\ell}_2, \boldsymbol{\ell}_3, \boldsymbol{\ell}_4, \boldsymbol{\ell}_5, \boldsymbol{\ell}_6) \delta_{\text{D}}(\boldsymbol{\ell}_1 + \boldsymbol{\ell}_2 + \boldsymbol{\ell}_3) \delta_{\text{D}}(\boldsymbol{\ell}_4 + \boldsymbol{\ell}_5 + \boldsymbol{\ell}_6)$ for some function f . However, this is impossible unless G_A is proportional to a Dirac function. Therefore, Eq. (52) cannot hold, and $C_{\langle M_{\text{ap}}^3 \rangle}$ and C_B are not related by simple integration.

Under the large-field approximation, though, Eq. (52) can be used. We show this in Appendix D, where we start from the Gaussian bispectrum covariance from Joachimi et al. (2009) to recover $T_{PPP,1}^{\infty}$.

5. Validation of model covariance

We test the analytical model for $C_{\hat{M}_{\text{ap}}^3}$ by comparing it to numerical estimates from mock data. This section describes the used data, measurement method, and results.

5.1. Validation data

We use two kinds of mock data: Shear maps for Gaussian density distributions and realistic shear and convergence maps from two cosmological N -body simulations, namely the Scinet Lightcone Simulations (SLICS, Harnois-Déraps & van Waerbeke 2015) and the suite by Takahashi et al. (2017, T17 hereafter). The data from N -body simulations are the same as for Paper I, which we describe here again for convenience.

5.1.1. SLICS

The SLICS contain 1536³ particles inside a 505 h^{-1} Mpc box. They are gravitationally evolved according to a flat Λ CDM cosmology with normalised Hubble constant $h = 0.69$, matter clustering parameter $\sigma_8 = 0.83$, matter density parameter $\Omega_{\text{m}} = 0.29$, baryon density parameter $\Omega_{\text{b}} = 0.047$, and primordial power spectrum spectral index $n_{\text{s}} = 0.969$. We use two different sets of data products from these simulations. The first consists of mock shear catalogues from 924 pseudo-independent lines-of-sight, each with a square area of 100 deg². The source galaxies are distributed with a redshift distribution of

$$n(z) \propto z^2 e^{-(z/z_0)^\beta}, \quad (54)$$

with $z_0 = 0.637$, $\beta = 1.5$ and normalisation such that the overall galaxy density is 30 arcmin⁻². This redshift distribution and number density correspond to expectations for stage IV surveys. The shear catalogues are infused with shape noise by adding random ellipticities from a Gaussian. We use a two-component ellipticity dispersion of $\sigma_\epsilon^2 = (0.37)^2$.

The second set of data products from the SLICS are shape noise-free convergence maps. These convergence maps have the same area and cosmology as the shear lines-of-sight, but they were obtained with all source galaxies situated at redshift $z_{\text{s}} = 1$.

KiDS-1000

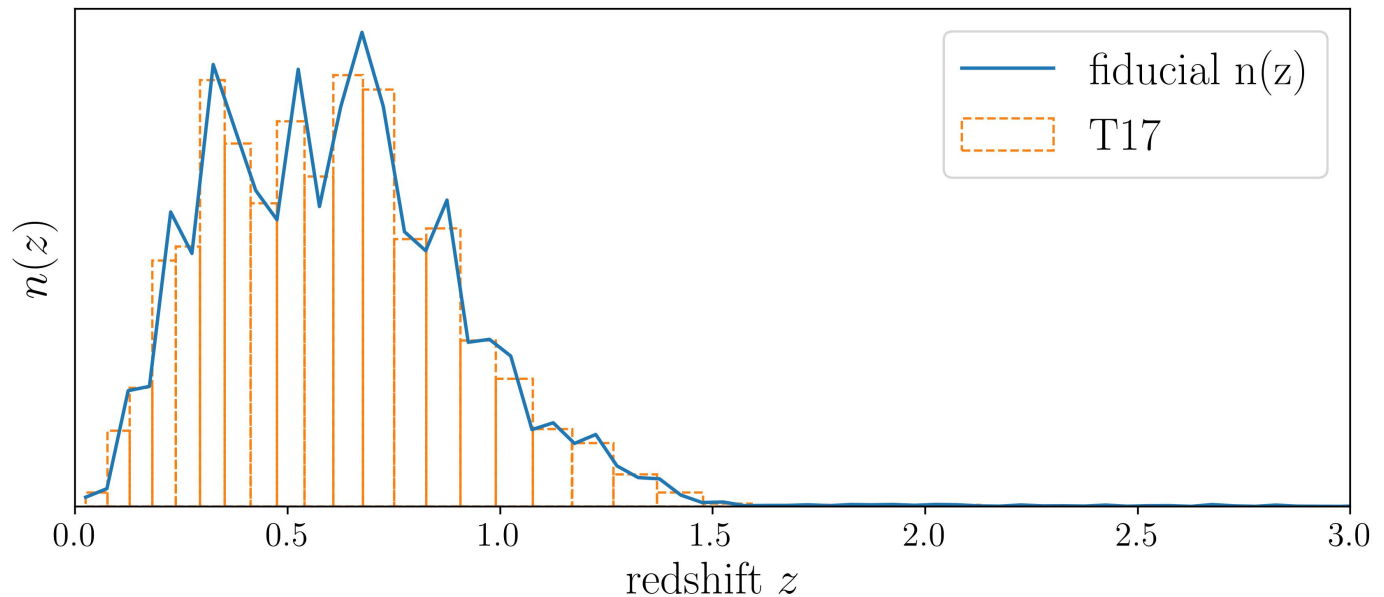


Fig. 3: Redshift distribution constructed from the T17 simulation given the fiducial $n(z)$ of the KiDS-1000 data.

5.1.2. T17 Simulations

The T17 simulations contain 2048^3 particles in a box of $450 h^{-1}$ Mpc. Each box is replicated eight times and placed around the observer using periodic boundary conditions. The particles are then evolved using GADGET2 (Springel et al. 2001) and a flat Λ CDM cosmology with parameters $h = 0.7$, $\sigma_8 = 0.82$, $\Omega_m = 0.279$, $\Omega_b = 0.046$, and $n_s = 0.97$. Using GRayTrix¹, light rays are traced through 108 realisations of the simulation, creating full-sky convergence shells at 38 redshifts.

We create mock data similar to the KiDS-1000 data release of the Kilo Degree Survey (KiDS, Kuijken et al. 2015) from these convergence shells by cutting out an area of 859.4 deg^2 from the convergence shells, combining them according to the KiDS-1000 $n(z)$ shown in Fig. 3, and adding a realistic shape noise with a standard deviation

$$\sigma = \frac{\sigma_\epsilon}{\sqrt{2n_{\text{gal}} A_{\text{pix}}}}, \quad (55)$$

with the pixel area A_{pix} , $n_{\text{gal}} = 6.17 \text{ arcmin}^{-2}$, and $\sigma_\epsilon = 0.375$.

5.1.3. Gaussian random fields (GRFs)

We also generate shear maps for Gaussian density distributions, characterised solely by their power spectrum. We use a shape-noise-free cosmic shear power spectrum based on the nonlinear matter power spectrum from the revised halofit prescription (Takahashi et al. 2012). We use the cosmological parameters of the T17 simulations and the KiDS-1000 $n(z)$.

From the power spectrum, we create square maps of the shear γ using the python library lenstools (Petri 2016) with the assumption of periodic boundary conditions. We create 4096 realizations for each of the sidelengths $\vartheta'_{\text{max}} \in \{10^\circ, 15^\circ, 20^\circ\}$. Each map contains $N_{\text{pix}} = 4096 \times 4096$ pixels.

5.2. Covariance estimation from data

We estimate the covariance of \hat{M}_{ap}^3 in three ways from the validation data. In the first method, we measure the aperture statistics $\langle M_{\text{ap}}^3 \rangle$ on all simulation realisations using FFT and then use the sample covariance as an estimate. In the second method, we measure the third-order shear correlation functions Γ_i and convert them to estimates of $\langle M_{\text{ap}}^3 \rangle$ for all simulation realisations. Finally, in the third method, we measure the aperture mass correlation functions and convert them to the terms $T_{PPP,1}$ to T_{P_6} (see Sect. 3.3).

¹ <http://th.nao.ac.jp/MEMBER/hamanatk/GRayTrix/>

5.2.1. Using FFT

The measurement of $\langle M_{\text{ap}}^3 \rangle$ in the simulations uses the same setup as the method described in [Paper I](#). We will summarise it here shortly. For the flat GRFs and the SLICS, we measure $C_{\hat{M}_{\text{ap}}^3}$ in the shear maps in three steps.

At first, we measure $M_{\text{ap}_i}(\boldsymbol{\vartheta}, \theta)$ for each realisation i , using scale radii $\theta \in \{4', 8', 16'\}$ for the SLICS and $\theta \in \{4', 8', 16', 32'\}$ for the GRFs. We use Eq. (7), which we evaluate with FFT. To remove edge effects, we cut off a border of 4 times the largest aperture radius, i.e. $4 \times 32' = 128'$ for the GRFs and $4 \times 16' = 64'$ for the SLICS, from each side of the M_{ap_i} -maps. This large cut-off is needed because our filter function Q_θ has infinite support and is significantly non-zero even for $\vartheta > \theta$. The filter contains 99.9% of its power within 4θ , so with the cut-off, boundary effects are negligible. The resulting M_{ap_i} -maps have side lengths $\vartheta_{\text{max}} \in \{5^\circ 73, 10^\circ 73, 15^\circ 73\}$ for the GRFs and $7^\circ 87$ for the SLICS.

Then, we estimate $\langle M_{\text{ap}}^3 \rangle_i$ for each realisation i . For this, we multiply $M_{\text{ap}_i}(\boldsymbol{\vartheta}, \theta_1)$, $M_{\text{ap}_i}(\boldsymbol{\vartheta}, \theta_2)$, and $M_{\text{ap}_i}(\boldsymbol{\vartheta}, \theta_3)$ and then average over $\boldsymbol{\vartheta}$. Finally, we estimate the measured covariance $C_{\hat{M}_{\text{ap}}^3}^{\text{meas}}$ with

$$C_{\hat{M}_{\text{ap}}^3}^{\text{sim}}(\Theta_1, \Theta_2) = \frac{1}{N-1} \sum_{i=1}^N \langle M_{\text{ap}}^3 \rangle_i(\theta_1, \theta_2, \theta_3) \langle M_{\text{ap}}^3 \rangle_i(\theta_4, \theta_5, \theta_6) \quad (56)$$

$$- \frac{1}{N(N-1)} \sum_{i=1}^N \langle M_{\text{ap}}^3 \rangle_i(\theta_1, \theta_2, \theta_3) \sum_{j=1}^N \langle M_{\text{ap}}^3 \rangle_j(\theta_4, \theta_5, \theta_6).$$

For the curved-sky T17 convergence maps, we smooth the maps with the `healpy` function `smoothing` with a beam window function determined by the corresponding U_θ filter for the same aperture radii as for the GRFs, i.e. $\theta \in \{4', 8', 16', 32'\}$. Each filter yields a full-sky aperture mass map M_{ap_i} , from which we extracted 18 tiles that are not adjacent. This gives in total 1944 almost independent realisations.

We compute uncertainty estimates with bootstrapping for both the SLICS and the T17 covariances from FFT. For this, we generate 10 000 vectors containing N_{real} randomly drawn integers between 1 and N_{real} where N_{real} is the number of realisations (924 for the SLICS and 1944 for the T17). The vectors can explicitly contain the same integer multiple times. For each vector, we take the $\langle M_{\text{ap}}^3 \rangle_i$ for which i is an element in the vector and use it to calculate a sample covariance with Eq. (56). In this way, we obtain 10 000 covariance estimates. We take the standard deviation of these estimates as uncertainty for the $C_{\hat{M}_{\text{ap}}^3}^{\text{sim}}$.

5.2.2. Using third-order shear correlation functions

As mentioned in Sect. 2, $\langle M_{\text{ap}}^3 \rangle$ is related to the natural components Γ_i of the third-order shear correlation function (see also Section 5.3 in [Paper I](#)). Therefore, we can estimate the $\langle M_{\text{ap}}^3 \rangle_i$ of each simulation realisation i by first measuring the Γ_i and then converting them to $\langle M_{\text{ap}}^3 \rangle_i$, following Equations (69) and (71) of [Schneider et al. \(2005\)](#). The covariance of \hat{M}_{ap}^3 can then be estimated as the sample variance of the $\langle M_{\text{ap}}^3 \rangle_i$, using Eq. (56).

We expect the covariance estimate from this approach to be smaller than the estimate from the FFT-based method described in the previous subsection. This is because, here, we do not cut off the border of the survey area. Consequently, more shear information is used to estimate $\langle M_{\text{ap}}^3 \rangle$, leading to a smaller covariance.

The measurement of the Γ_i is very time-intensive. Therefore, we restrict this approach to the SLICS data, where we measure the Γ_i using `treecorr` ([Jarvis et al. 2004](#)). We use 10 bins each for the triangle parameters u, v , and r with r between $0'.1$ and $120'$. As shown in [Paper I](#), binning the Γ_i in this way yields accurate $\langle M_{\text{ap}}^3 \rangle$ for scale radii between $4'$ and $16'$.

5.2.3. Using aperture mass correlation functions

As shown in Sect. 3.3, the individual terms of the covariance can be estimated from the aperture mass correlation functions which we use to validate the analytic expressions.

For this, we measure the aperture mass maps $M_{\text{ap}_i}(\boldsymbol{\vartheta}, \theta)$ according to Sect. 5.2.1. From these maps, we first calculate the $M_{\text{ap}_i}(\boldsymbol{\vartheta}, \theta_1)M_{\text{ap}_i}(\boldsymbol{\vartheta}, \theta_2)$ and $M_{\text{ap}_i}(\boldsymbol{\vartheta}, \theta_1)M_{\text{ap}_i}(\boldsymbol{\vartheta}, \theta_2)M_{\text{ap}_i}(\boldsymbol{\vartheta}, \theta_3)$ by multiplying the aperture mass maps for different filter radii. Then, we estimate the correlation functions $M_{\text{ap}}^{2,1}(\theta_1; \theta_2; \eta)$, $M_{\text{ap}}^{3,1}(\theta_1, \theta_2; \theta_3; \eta)$, $M_{\text{ap}}^{4,3}(\theta_1, \theta_2, \theta_3; \theta_4; \eta)$, and $M_{\text{ap}}^{4,2}(\theta_1, \theta_2; \theta_3, \theta_4; \eta)$ by correlating the relevant aperture mass maps: We first extend the fields $M_{\text{ap}_i}(\boldsymbol{\vartheta}, \theta)$ using zero-padding, meaning that we add pixel grids containing only zeros to the boundary of the map. Doing this, $M_{\text{ap}_i}(\boldsymbol{\vartheta}, \theta)$ becomes $W_A(\boldsymbol{\vartheta})M_{\text{ap}_i}(\boldsymbol{\vartheta}, \theta)$. The correlation between two aperture mass maps then yields

$$\int_A d^2\vartheta W_A(\boldsymbol{\vartheta}) M_{\text{ap}_i}(\boldsymbol{\vartheta}, \theta_1) W_A(\boldsymbol{\vartheta} + \boldsymbol{\eta}) M_{\text{ap}_i}(\boldsymbol{\vartheta} + \boldsymbol{\eta}, \theta_2) = E(\boldsymbol{\eta}) M_{\text{ap}}^2(\theta_1, \theta_2; \boldsymbol{\eta}). \quad (57)$$

We perform this correlation using the `correlate2D` function from `scipy`. Finally, we calculate the terms $T_{PPP,1}$ to T_{P_6} with the expressions in Sect. 3.3.

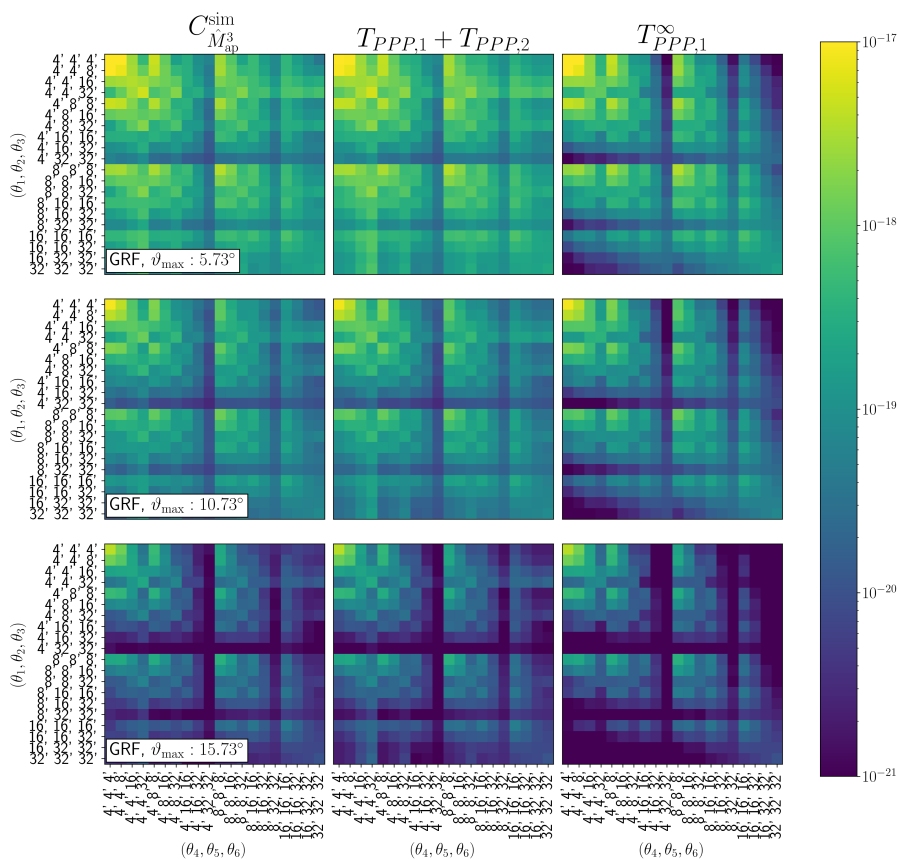


Fig. 4: $C_{M_{\text{ap}}}^3$ for the GRF, each row is showing a different field size. In the left column are the measured $C_{M_{\text{ap}}}^3$ from the simulated GRF. The middle column shows the model prediction, including the finite-field term $T_{PPP,2}$. The covariances under the large-field approximation, for which $T_{PPP,2}$ vanishes, are in the right column.

Our method to measure the correlation function uses the flat-sky approximation, so we did not apply it to the T17 simulations. Furthermore, the correlation function estimation of the terms $T_{PPP,2}$ and $T_{PT,2}$ is strongly affected by noise, which is why we only use it for the SLICS without shape noise.

5.3. Results

5.3.1. Gaussian random fields

We compare the covariance for $\langle M_{\text{ap}}^3 \rangle$ measured in the simulated GRFs with the analytical expression $T_{PPP,1} + T_{PPP,2}$ and the large-field approximation $T_{PPP,1}^{\infty}$ in Fig. 4. We note that for the GRFs, all terms containing the bi-, tri-, or pentaspectrum vanish, so the middle column gives the full analytical prediction for the covariance. We see that, as expected, both simulated and analytical covariance decrease with increasing survey size. The full analytic covariance shows similar values to the simulated covariance for all combinations of aperture radii. The large-field approximation agrees only on and near the diagonal with the simulation and is much smaller for elements far from the diagonal.

This observation is quantified in Fig. 5, where we show the fractional differences between the simulated and analytically calculated covariances. The full analytical expression shows deviations of less than 30% to the simulation, while the large-field approximation is almost a factor of two too small for the non-diagonal elements. While the deviations decrease with field size, they are still significant for the largest side length of 15.73 . Consequently, neglecting $T_{PPP,2}$ is inappropriate, even for surveys of a size of $(15.73)^2 = 247.43 \text{ deg}^2$.

The remaining disagreement between the full analytic covariance model and the simulations can be explained by the discreteness of the shear maps. Due to the finite pixel number, the shear maps contain only modes which are $\ell = 2\pi \sqrt{i^2 + j^2} / \vartheta'_{\text{max}}$, where i and j are integers between 0 and $N_{\text{pix}}/2$, where N_{pix} is the pixel number and ϑ'_{max} is the side length of the shear maps (before boundary cut-off). Therefore, while the model assumes a smooth power spectrum $P(\ell)$, the actual power spectrum of the GRF is

$$P^{\text{GRF}}(\boldsymbol{\ell}) = \left(\frac{2\pi}{\vartheta'_{\text{max}}} \right)^2 \sum_{i=1}^{N_{\text{pix}}/2} \sum_{j=1}^{N_{\text{pix}}/2} P \left(\frac{2\pi \sqrt{i^2 + j^2}}{\vartheta'_{\text{max}}} \right) \delta_{\text{D}} \left(\ell_1 - \frac{2\pi i}{\vartheta'_{\text{max}}} \right) \delta_{\text{D}} \left(\ell_2 - \frac{2\pi j}{\vartheta'_{\text{max}}} \right), \quad (58)$$

with $\boldsymbol{\ell} = (\ell_1, \ell_2)$. Due to the large pixel number, it is not feasible to directly calculate $T_{PPP,1}$ and $T_{PPP,2}$ for this power spectrum. However, using P^{GRF} is similar to assuming that P is zero for ℓ outside of $[\ell_{\text{min}}, \ell_{\text{max}}]$, with $\ell_{\text{min}} = 2\pi/\vartheta'_{\text{max}}$, and $\ell_{\text{max}} = \pi N_{\text{pix}}/\vartheta'_{\text{max}}$. This is the same as increasing the lower and decreasing the upper integration boundary for the

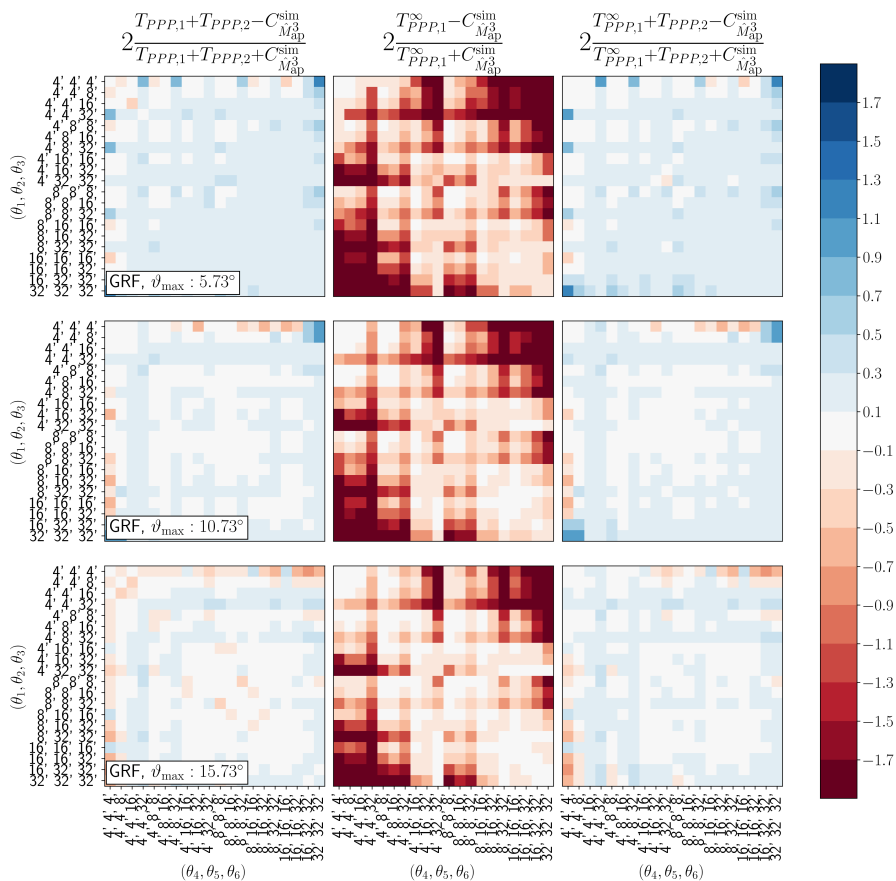


Fig. 5: Fractional differences of the model covariance to the measured $C_{M_{\text{ap}}^3}$ for the GRF, each row showing a different field size. In the left column are the fractional differences between the full analytic model and the simulated GRF. The middle column shows the difference between the large-field approximation, neglecting the finite field term, and the simulated covariance. In the right column, the difference of the model using the large-field approximation for $T_{PPP,1}$, but keeping $T_{PPP,2}$ as it is, is shown.

ℓ -integrals in $T_{PPP,1}$ and $T_{PPP,2}$. We show the impact of these integration borders in Fig. 6. The upper boundary ℓ_{max} , and consequently the pixel number, has only a small impact on the model covariance. This is because the aperture filters \hat{u} decrease with ℓ and are already small at $\ell \simeq \ell_{\text{max}}$. The lower boundary ℓ_{min} has a stronger impact. By increasing the lower integration border to ℓ_{min} , we decrease the model covariance. This decrease significantly improves the agreement between the simulated GRFs and the model.

As the field size (and ϑ'_{max}) increases, ℓ_{min} decreases so that smaller ℓ -modes are included in the GRFs. Therefore, the difference between the model, evaluated for all ℓ , and the covariance from the GRF shrinks with increasing field size, as seen in the right column of Fig. 5.

We also show in Fig. 5 the fractional difference between $T_{PPP,1}^{\infty} + T_{PPP,2}$ and the simulated covariance. This approximated analytic expression shows a similar level of agreement with the simulated covariance as the full expression. The cause of this good agreement is the similarity between $T_{PPP,1}$ and $T_{PPP,1}^{\infty}$, shown in Fig. 7. Even for the smallest field size with side length $\vartheta_{\text{max}} = 5.73$, most elements of $T_{PPP,1}$ and $T_{PPP,1}^{\infty}$ differ by less than 5%, with stronger deviations mostly at very large aperture radii ($32'$) or very small aperture radii ($4'$). For the largest field, all elements agree at better than 15%.

The agreement between $T_{PPP,1}$ and $T_{PPP,1}^{\infty}$ encourages a practical simplification, which is substituting $T_{PPP,1}$ by the large-field approximation. This significantly simplifies the calculation: Equation (43) to obtain $T_{PPP,1}^{\infty}$ contains only three integrals, while Eq. (20) for $T_{PPP,1}$ contains six integrals, two of which involve oscillating functions. Consequently, the numerical integration for $T_{PPP,1}^{\infty}$ is much simpler and faster.

The finite field effect, which gives rise to $T_{PPP,2}$, can be important for covariance estimates derived from simulations. Such estimates are sometimes performed on simulations with a smaller area than the survey to which the covariance is applied. To account for the different areas, the covariances are rescaled by a factor $A_{\text{sim}}/A_{\text{survey}}$, where A_{sim} and A_{survey} are the simulation and survey areas, respectively. This rescaling assumes that the covariance is inversely proportional to the survey area, which is only true under the large-field approximation. While $T_{PPP,1}^{\infty}$ indeed scales with the inverse survey area, $T_{PPP,2}$ decreases faster, as shown in Sect. 3.4. We demonstrate the failure of the rescaling approach in Fig. 8, where we show the fractional difference between the covariance for the simulated GRF with a side length of 15.73 and the analytical estimate for the side length 5.73 , rescaled by the factor $(5.73/15.73)^2$. The rescaled covariance is too large by a factor of up to 4.7.

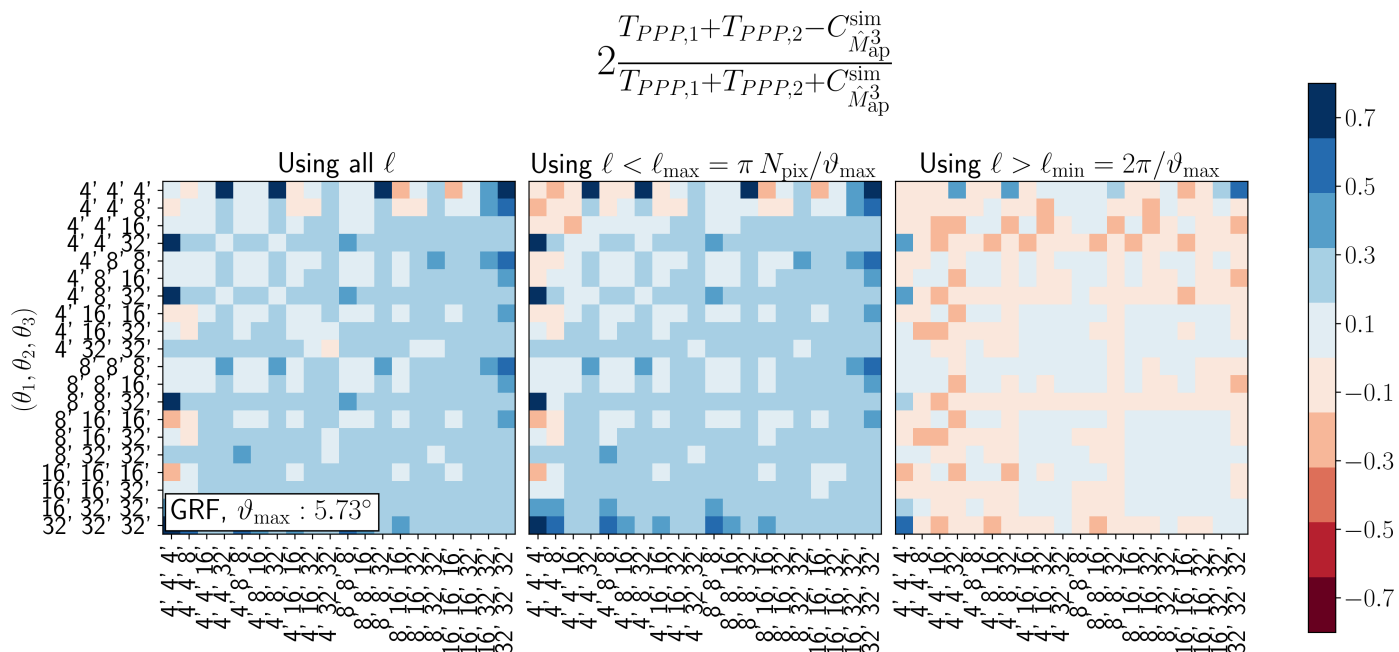


Fig. 6: Fractional differences between covariance model and estimate from GRFs with $\vartheta_{\max} = 5.78$ for different choices of the boundaries of the ℓ -integrals. Left: Fiducial calculation of model, where $P(\ell)$ is used for all ℓ . Middle: ℓ -modes larger than ℓ_{\max} are cut-off. This removes modes not present in the simulation due to the finite pixel size. Right: ℓ -modes smaller than ℓ_{\min} are cut-off. This removes modes not present in the simulation due to the finite field size.

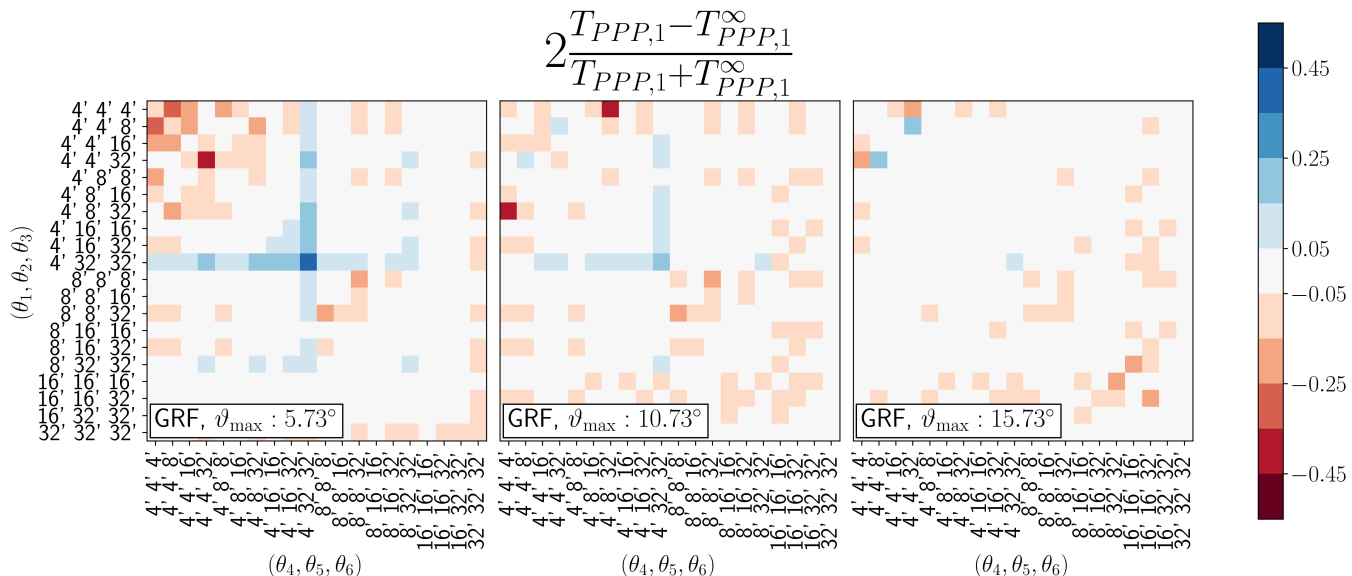


Fig. 7: Fractional differences of $T_{PPP,1}$ with and without large-field approximation for different field sizes

5.3.2. N -body simulations

We now compare the full analytic $C_{M_{ap}^3}$, including the non-Gaussian terms, to the covariances from the N -body simulations. Figure 9 compares the $C_{M_{ap}^3}$ and $C_{M_{ap}^3}^{\text{sim}}$ for the SLICS and the T17 simulations. For the SLICS, we see deviations of 1 to 2 times the simulation uncertainty, with the model being larger than the simulated covariance at most scales. These deviations could indicate that the power-, tri-, and pentaspectrum of the SLICS do not correspond to the model polyspectra. This could be caused by the finite resolution and smoothing in the simulations, the need for additional halo terms for the tri- and pentaspectrum in the model, or the general inaccuracy of the halo model. However, for the T17,

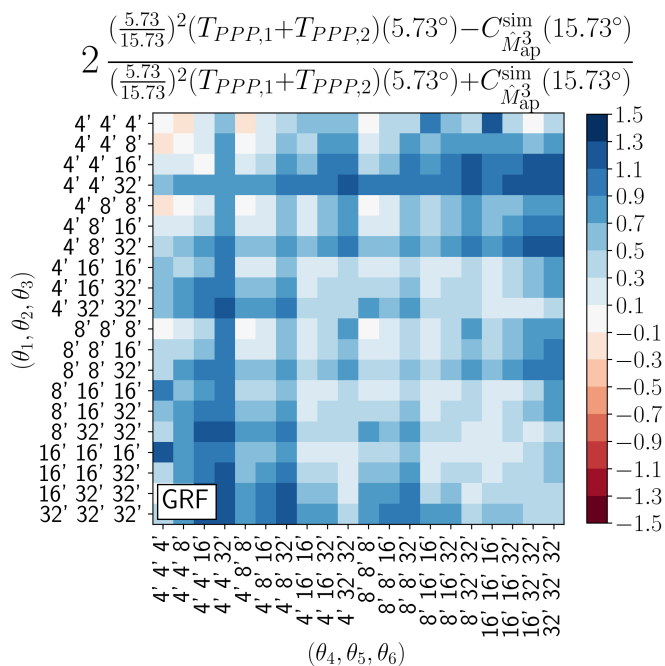


Fig. 8: Fractional difference of model covariance, rescaled from a field size of $5:73^2$ to $15:73^2$ to the covariance from a simulated GRF of size $15:73^2$. The rescaling is performed under the assumption that the covariance scales inversely proportional to the survey area, which is not true for the finite field term $T_{PPP,2}$.

we generally see a better agreement between simulation and model. Most elements agree within the simulation accuracy, with a few elements outside the 2σ range.

We compare the diagonals of the individual terms of the analytic covariance in Fig. 10. We see that for both the SLICS and T17 setup, the non-Gaussian terms are dominant. For the SLICS, T_{P_6} dominates on all scales, whereas for the T17, the first Gaussian term $T_{PPP,1}$ is of a similar magnitude as T_{P_6} . This difference is caused by the different levels of shape noise in the two simulations. For the SLICS, we use a Stage-IV-like setup, where the galaxy number density is $n_g = 30 \text{ arcmin}^{-2}$, while the T17 use the KiDS-like number density of $n_g = 6.17 \text{ arcmin}^{-2}$. Therefore, the Gaussian covariance term for the T17 has a larger impact than for the SLICS.

As mentioned before, we can also directly measure the individual covariance terms and compare them to the analytic prediction in Fig. 11 using aperture mass correlation functions. Unfortunately, measuring the finite-field terms $T_{PPP,2}$ and $T_{PT,2}$ is challenging: In Eqs. (36) and (39) one can see that, when neglecting the function $E_A(\boldsymbol{\eta})$, the integral over the correlation function is, by definition, zero. So the only part that leads to $T_{PPP,2}$ and $T_{PT,2}$ being non-zero is multiplication with the slowly varying function $E_A(\boldsymbol{\eta})$. This amplifies the effect of noise in the measured correlation function. Thus, the measurements of $T_{PPP,2}$ and $T_{PT,2}$ are very sensitive to the noise level, and we can only perform them in the SLICS without shape noise. The measured and modelled covariance terms show similar dependencies on the aperture scale radii. The model for the dominating term T_{P_6} agrees within a few per cent with the measurement. For $T_{PPP,1}$, $T_{PPP,2}$, and $T_{PT,2}$, though, the model underpredicts the measurements. This difference is likely due to differences between the model polyspectra and the actual polyspectra of the simulation. Since our trispectrum model contains only the 1-halo term, we do not expect a perfect match between the modelled $T_{PT,1}$ and $T_{PT,2}$ and the measurement. Furthermore, the BiHalofit bispectrum model only agrees with the data at the 10% level, (compare to Appendix A of Paper I), so deviations at the 20% level are expected for T_{BB} , which depends on the square of the bispectrum.

The term $T_{P_6,2h}$ gives a significant contribution to T_{P_6} . We show this in Fig. 12, where the blue line shows the diagonal of the ratio between $T_{P_6,2h}$ and $T_{P_6}^\infty + T_{P_6,2h}$ for the T17 setup. The two-halo term is substantial for small apertures and the combinations of small and large apertures. The figure also shows the same ratio for larger field sizes. The importance of $T_{P_6,2h}$ decreases with field size. This is as expected, since $T_{P_6}^\infty$ scales with the inverse survey area, while $T_{P_6,2h}$ decreases faster.

Finally, we compare the covariance estimated in the SLICS using the shear three-point correlation function Γ_i to the FFT-based estimate in Fig. 13. We also show the model prediction for two different survey areas: either the entire survey area of $10^\circ \times 10^\circ$ or the survey area of $7:87 \times 7:87$ after boundary removal. As expected, the FFT-based covariance estimate is larger than the Γ_i -based estimate. This is a direct consequence of the boundary removal for the FFT - the effective survey area shrinks.

The Γ_i -based covariance is itself larger than the full-survey model covariance. This is because, as mentioned before, estimates of $\langle M_{ap}^3 \rangle$ for the whole survey area A' require shear information outside of A' . Consequently, unbiased estimates of $\langle M_{ap}^3 \rangle$ on A' contain more information than estimates of Γ_i , which are restricted to A' . Therefore, the covariance of the Γ_i -based estimator lies in between the model covariance for the total area A' and cut-off survey area A . Since the Γ_i -based estimator is required to analyse survey data, the covariance model gives an upper and lower bound to the expected survey constraints.

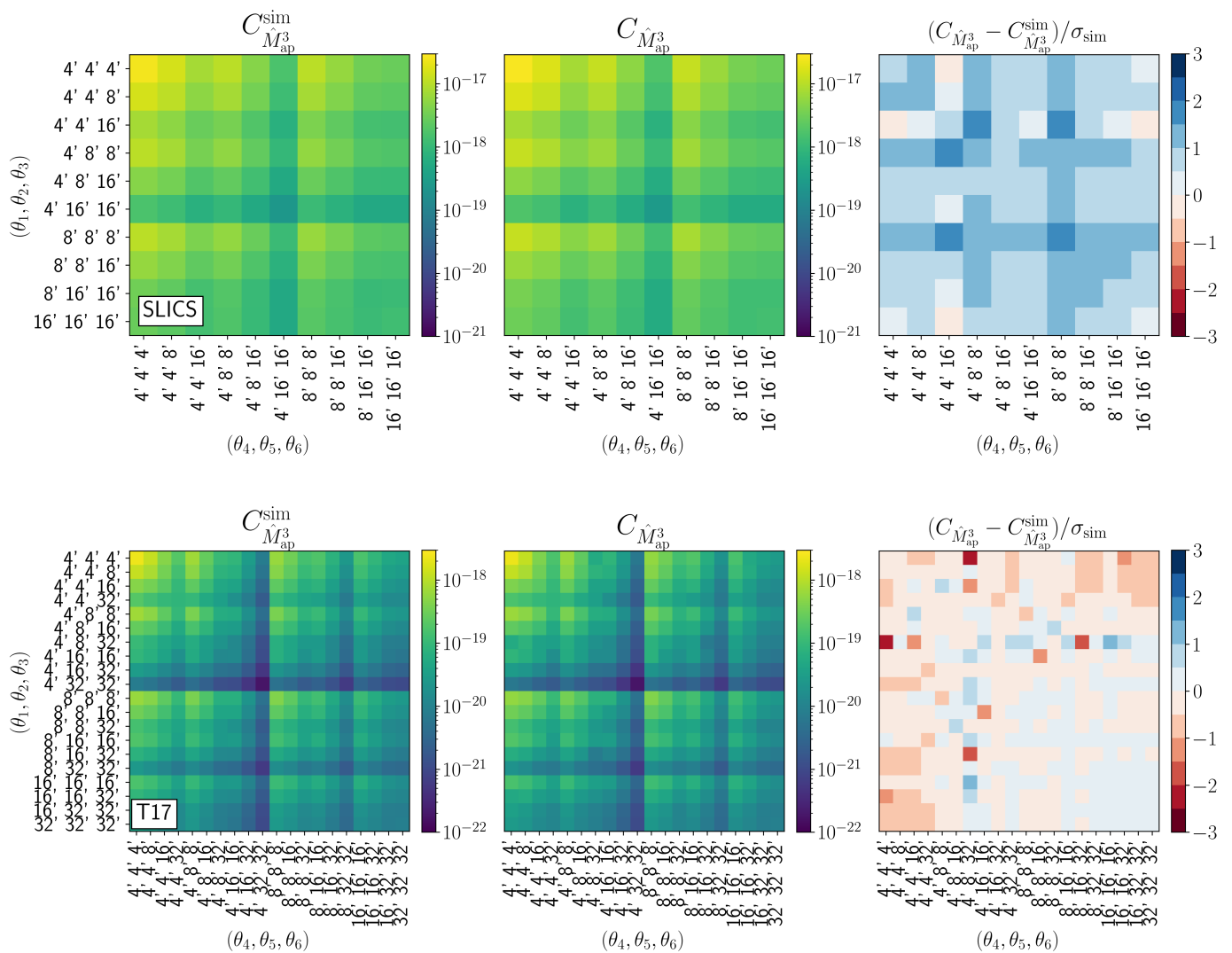


Fig. 9: Comparison of measured and modelled covariance for the SLICS (top) and T17 simulations (bottom). Left are the measured covariance, in the middle are the model predictions; right are the differences between model and simulation, normalized by the simulation bootstrap error.

6. Influence of covariance terms on cosmological parameter estimation

We have shown in the previous section that the analytical covariance estimates agree with estimates from the simulations within 1–2 times the simulations’ statistical uncertainty. However, it is unclear whether this level of agreement is sufficient for a cosmological parameter analysis. To test this, in this section, we perform mock MCMC analyses using $C_{\hat{M}_{ap}^3}$ and $C_{M_{ap}^3}^{sim}$, and compare the resulting parameter constraints. We also test the impact of the individual covariance terms on the cosmological analysis.

6.1. Analysis setup

We perform mock cosmological analyses with the same setup as in Paper I. In this setup, we use the neural network emulator *CosmoPower* (Spurio Mancini et al. 2022) to quickly evaluate the $\langle M_{ap}^3 \rangle$ model and sample the parameter likelihood. With the trained emulator, we evaluate the parameter likelihoods for different choices for the covariance: the estimate from the simulations, the full analytic expressions, and various combinations of the individual terms of $C_{\hat{M}_{ap}^3}$. Since the $\langle M_{ap}^3 \rangle$ are not sensitive to w_0 and h in a non-tomographic setting, we evaluate the likelihood for fixed $w_0 = -1$ and $h = 0.69$. For the T17 validation, we evaluated the $\langle M_{ap}^3 \rangle$ -model at the aperture scale radii 4’, 8’, 16’, and 32’, whereas for the SLICS setup we used the aperture scale radii 4’, 8’, and 16’. The reference data vector is measured at the corresponding cosmology of the respective simulation.

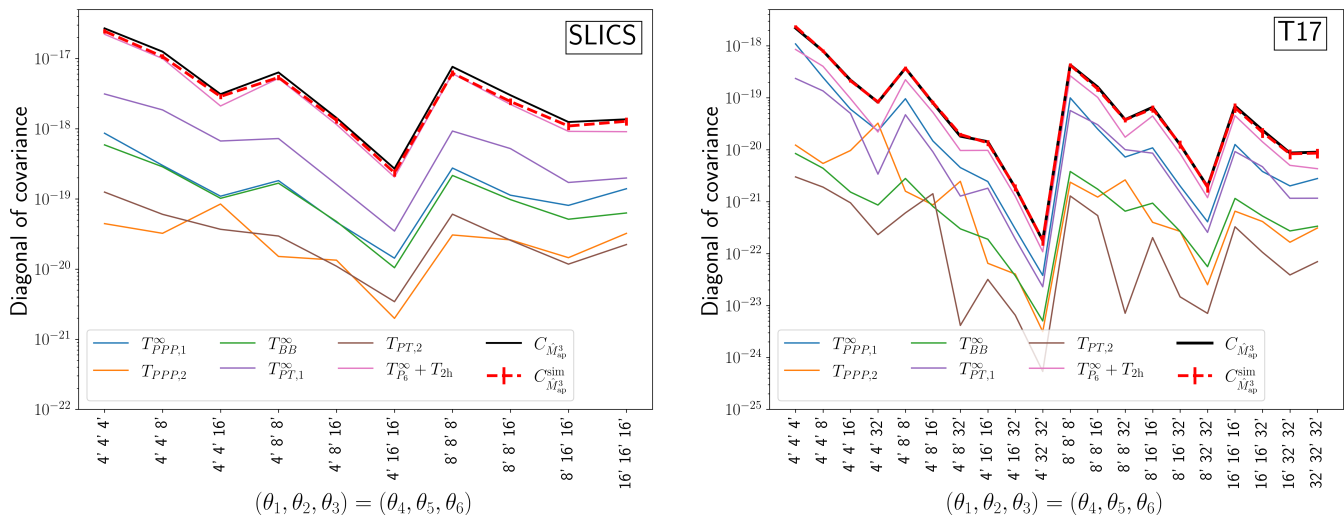


Fig. 10: Diagonal of $C_{M_{\text{ap}}}^3$ and the individual covariance terms for the SLICS (left) and the T17 (right). The measurement from the simulation is shown as a red dashed line, while the full modelled $C_{M_{\text{ap}}}^3$ is the bold black line. The other lines show individual terms. Error bars on the simulated covariances originate from bootstrapping

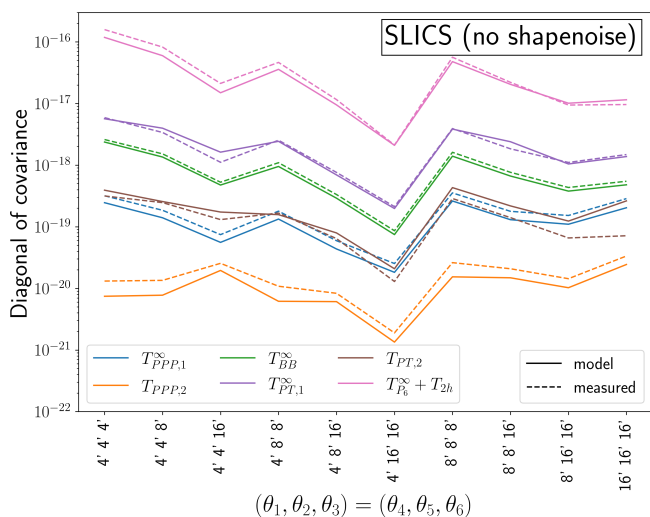


Fig. 11: Comparison of individual covariance terms modelled (solid) and measured (dashed) in the SLICS without shape noise.

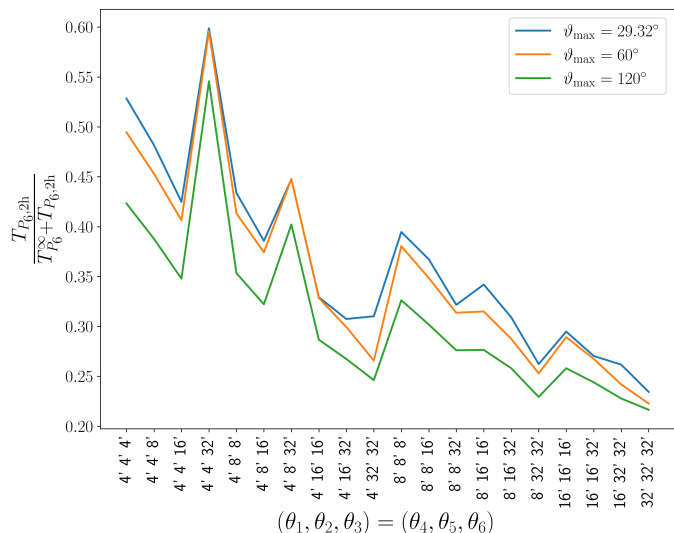


Fig. 12: Ratio of two-halo contribution $T_{P_6,2h}$ to full T_{P_6} term for various field sizes with T17 cosmology. The blue line corresponds to the KiDS1000-like field size.

6.2. Results

In Fig. 14a, we show the T17 results for the constraints on Ω_m , S_8 , and σ_8 , while varying only Ω_m and S_8 . In Table 1 we report the resulting marginalised parameter constraints together with the figure-of-merit (FoM) estimated as

$$\text{FoM} = \frac{1}{\sqrt{\det(C)}}, \quad (59)$$

where C is the parameter covariance matrix resulting from the MCMC process. The T17 covariances are tailored to a KiDS-like survey area and shape noise. The constraints from the simulated and analytic covariance coincide. The FoM of Ω_m – S_8 differs by less than 3%. Consequently, the analytic covariance is ideal for an unbiased cosmological analysis in our setup. We display in Fig. 14b the comparison for the SLICS setup. The posteriors for both the simulated and modelled covariance matrix clearly agree. This supports the robustness of the modelled covariance for varying survey areas, shape noise and redshift distribution.

In Fig. 15, we compare the parameter constraints obtained when using the total analytic covariance estimate, only the Gaussian terms $T_{PPP,1}$ and $T_{PPP,2}$, when neglecting the finite-field terms $T_{PPP,2}$ and $T_{PT,2}$, and when neglecting the term $T_{P_6,2h}$. The results demonstrate the importance of the non-Gaussian covariance terms, as the FoM of Ω_m – S_8

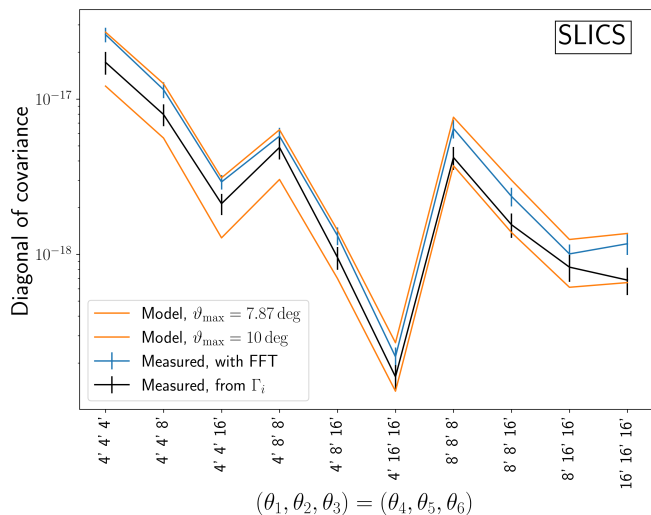


Fig. 13: Covariance in SLICS, measured with shear correlation functions Γ_i (black) and FFT (blue), as well as the model covariance for the full survey area of $10^\circ \times 10^\circ$ (orange, dashed) and for the effective survey area of $7.87^\circ \times 7.87^\circ$.

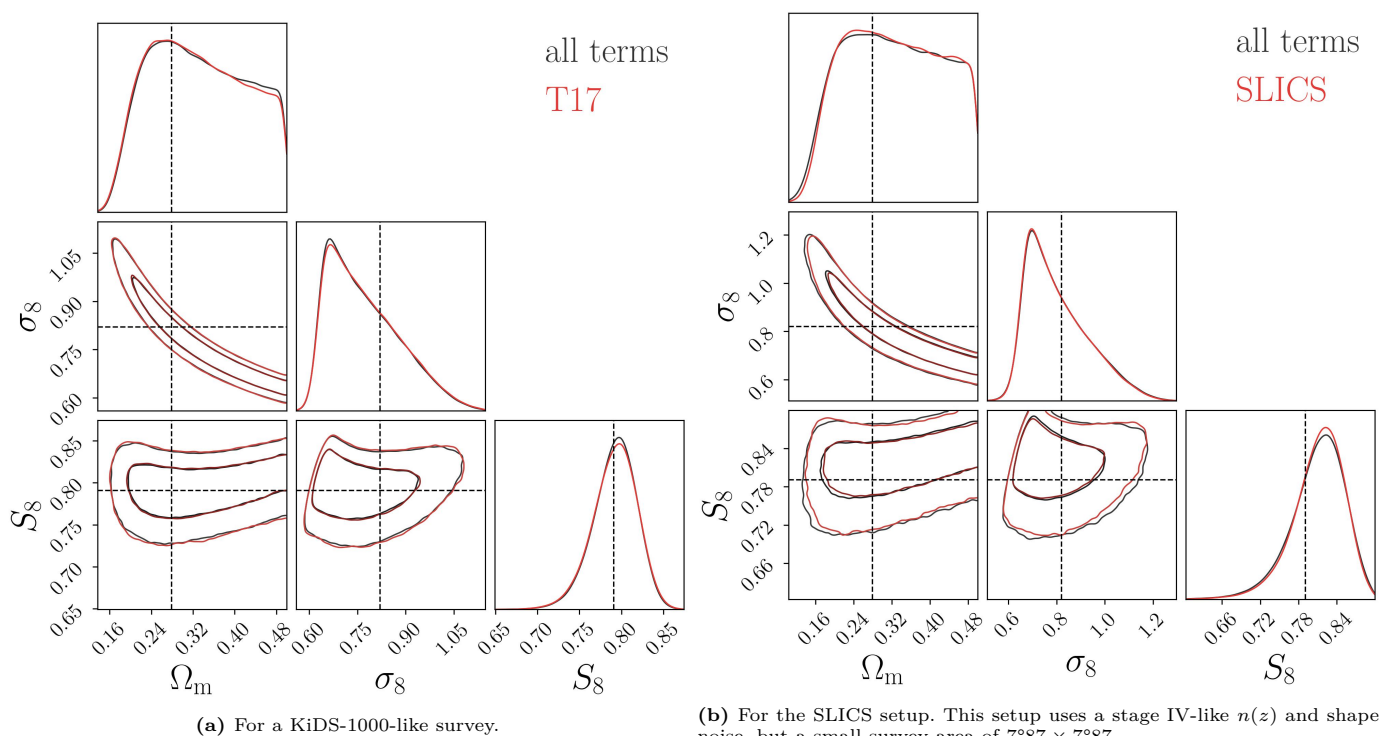


Fig. 14: Parameter constraints, using either the covariance from the simulations (red) or the analytic model (black).

approximately triples if only the Gaussian terms are used (see Table 1). Consequently, for the application to a Stage III survey, non-Gaussian covariance terms for $\langle M_{\text{ap}}^3 \rangle$ cannot be neglected.

For the KiDS-like survey area used here, the finite-field terms $T_{PPP,2}$ and $T_{PT,2}$ play a secondary role (see Table 1). The FoM of Ω_m - S_8 increases by 12% if these terms are neglected. Consequently, depending on the desired accuracy of the modelled covariance, these terms could be neglected for a real parameter analysis. Since calculating $T_{PPP,2}$ and $T_{PT,2}$ for a real survey requires evaluating Eq. (22) for the true, most likely complicated, survey geometry, bypassing them could significantly decrease the computational complexity of the covariance calculation. Ignoring $T_{P_{6,2h}}$, the 2-halo contribution to T_{P_6} , has a stronger effect. Neglecting $T_{P_{6,2h}}$ increases the FoM of Ω_m - S_8 by 27% and has a significant impact on the inferred constraints on the individual parameters.

7. Discussion

In this work, we derived an analytic model for the covariance of the third-order aperture statistics $\langle M_{\text{ap}}^3 \rangle$. We make our modelling code publically available at <https://github.com/sheydenreich/threepoint/releases>.

Table 1: Overview of the marginalised MAP values and 68% confidence intervals resulting from MCMC chains where Ω_m , S_8 are varied and $\sigma_8 = S_8 \sqrt{0.3/\Omega_m}$. We fixed $h = 0.7$ and $w_0 = -1$.

MAP	Ω_m	σ_8	S_8
T17	$0.272^{+0.148}_{-0.065}$	$0.665^{+0.173}_{-0.038}$	$0.798^{+0.023}_{-0.029}$
analytic model (all terms)	$0.259^{+0.166}_{-0.048}$	$0.661^{+0.172}_{-0.035}$	$0.798^{+0.023}_{-0.027}$
analytic model (all terms, without 2-halo term)	$0.260^{+0.170}_{-0.047}$	$0.663^{+0.166}_{-0.033}$	$0.798^{+0.021}_{-0.021}$
analytic model (neglecting finite-field terms)	$0.271^{+0.150}_{-0.061}$	$0.661^{+0.171}_{-0.033}$	$0.797^{+0.023}_{-0.025}$
analytic model (only Gaussian)	$0.271^{+0.132}_{-0.052}$	$0.664^{+0.164}_{-0.019}$	$0.795^{+0.015}_{-0.013}$
FoM	Ω_m - σ_8	Ω_m - S_8	σ_8 - S_8
T17	293	429	341
analytic model (all terms)	299	441	353
analytic model (all terms, without 2-halo term)	334	561	445
analytic model (neglecting finite-field terms)	321	482	388
analytic model (only Gaussian)	553	1216	966

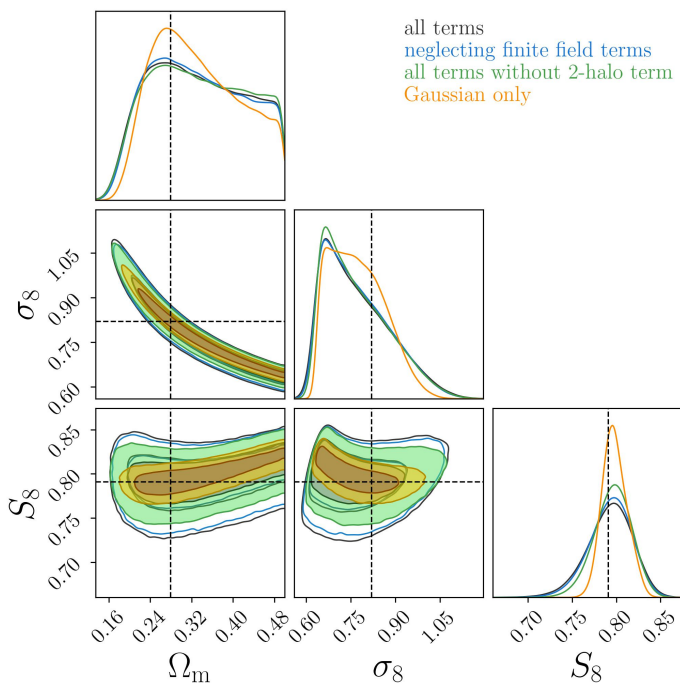


Fig. 15: Parameter constraints for a KiDS-1000-like survey, using the full model covariance (black), neglecting the finite field terms (blue), neglecting the 2-halo contribution to T_{P_6} (green) or using only the Gaussian covariance (orange). The FoMs of Ω_m - S_8 are given in Table 1.

We performed three tests for this analytic model. First, we compared the Gaussian part of the covariance to simulated GRFs. We found that all elements of the modelled covariance agree with the GRFs within 30%, with most elements agreeing better than 10% with the simulated data. Second, we compared the full model to two independent N -body simulations, the SLICS and T17 simulations. These comparisons showed that the model agrees within 1–2 times the statistical uncertainty on the simulations with the simulated covariance estimates. Third, we compared the expected constraints from a KiDS-1000-like survey for the cosmological parameters Ω_m and S_8 using the covariance from the T17 simulations and the analytic expression. The constraints were remarkably similar, with only a 3% deviation in the FoM on Ω_m - S_8 . These three tests confirmed that our covariance model is sufficiently accurate for analysing a stage III survey.

Additionally, we found that all terms of the \hat{M}_{ap}^3 covariance can be estimated by measuring aperture mass correlation functions. Using this approach, we compared the individual terms of the model to measurements in the SLICS and confirmed that the model agrees with the simulations.

In the derivation of the covariance model, we found terms that decrease faster than the inverse survey area and vanish entirely under the ‘large-field approximation’, which assumes an infinitely broad survey window function. These ‘finite-field terms’ show a complex dependence on the survey geometry, while the other terms mainly scale with the inverse survey area. The finite field term $T_{PPP,2}$ is already present in the Gaussian case. Comparing the model to GRFs showed that it is the dominating contribution for non-diagonal elements, and neglecting it leads to a severe bias. However, the

effect of the finite-field term is small for the realistic covariances, including non-Gaussianity, as they are dominated by the pentaspectrum term T_{P_6} . Ignoring the finite-field terms leads to an increment of only 12% in the FoM on Ω_m - S_8 .

We showed that it is incorrect to derive the covariance for the real-space statistic \hat{M}_{ap}^3 from a bispectrum covariance. Using an integral over a bispectrum covariance to model the covariance of \hat{M}_{ap}^3 is only possible under the large-field approximation. However, in this case, one automatically neglects the finite-field terms.

We note that our covariance model assumes the flat-sky approximation. Nevertheless, the favourable comparison to the T17 simulation indicates that this assumption is valid at the relatively small scales considered here. This is not a surprising finding since we consider $\langle M_{\text{ap}}^3 \rangle$ at small, sub-degree scales. At these small scales, the flat-sky approximation introduces no significant bias. Our model should therefore be applicable to actual observations.

Our covariance model is based on an estimator for $\langle M_{\text{ap}}^3 \rangle$ that is easily applicable to simulations but should not be applied to realistic survey data, which include masks, because it requires a continuous convergence (or shear) map. Instead, one must use an estimator based on the third-order shear correlation functions. However, we have shown that our model can quantify the covariance of this estimator. The model covariance for the entire survey area gives a lower bound to the expected covariance, while the model covariance for a smaller effective area after boundary removal gives an upper bound. For a square survey with an area of 1000 deg^2 and a boundary cut-off of $4 \times 16'$, the upper bound is around 15% above the lower bound, which gives relatively tight constraints on the true covariance. For even larger stage IV surveys, the bound will be tighter, as the boundary is a smaller fraction of the overall area.

In conclusion, we have presented and validated an analytic model for the covariance of third-order aperture statistics. Together with the analytical model for $\langle M_{\text{ap}}^3 \rangle$ presented in Paper I, our covariance model paves the way for the cosmological analysis of third-order shear statistics of stage III and stage IV weak lensing surveys.

We have deliberately avoided the term super-sample covariance (SSC) to describe parts of $C_{\hat{M}_{\text{ap}}^3}$. This term, originally devised for parts of the covariance of the power spectrum (Takada & Hu 2013), is used to describe covariance parts depending on ℓ -modes larger than a given survey area. The term $T_{P_6,2\text{h}}$ corresponds to what is commonly called SSC for the bispectrum (Chan et al. 2018; Pyne & Joachimi 2021). However, as we will show in a forthcoming paper, the SSC can be defined as the difference between the exact form of a covariance and its large-field approximation. By this definition, the finite-field terms $T_{PPP,2}$ and $T_{PT,2}$ are also part of the SSC for \hat{M}_{ap}^3 .

Acknowledgements. Funded by the TRA Matter (University of Bonn) as part of the Excellence Strategy of the federal and state governments. This work has been supported by the Deutsche Forschungsgemeinschaft through the project SCHN 342/15-1 and DFG SCHN 342/13. PAB and SH acknowledge support from the German Academic Scholarship Foundation. We would like to thank Joachim Harnois-Déraps for making public the SLICS mock data, which can be found at <http://slics.roe.ac.uk/>. We thank Benjamin Joachimi, Susan Pyne, Lucas Porth and Niek Wielders for many helpful comments and discussions.

References

- Abbott, T. M. C., Aguena, M., Alarcon, A., et al. 2022, *Phys. Rev. D*, 105, 023520
 Bartelmann, M. 2010, *Classical and Quantum Gravity*, 27, 233001
 Bartelmann, M. & Schneider, P. 2001, *Phys. Rep.*, 340, 291
 Burger, P. A., Friedrich, O., Harnois-Déraps, J., et al. 2022, arXiv:2208.02171
 Chan, K. C., Moradinezhad Dizgah, A., & Noreña, J. 2018, *Phys. Rev. D*, 97, 043532
 Cooray, A. & Sheth, R. 2002, *Phys. Rep.*, 372, 1
 Crittenden, R. G., Natarajan, P., Pen, U.-L., & Theuns, T. 2002, *ApJ*, 568, 20
 Friedrich, O., Andrade-Oliveira, F., Camacho, H., et al. 2021, *MNRAS*, 508, 3125
 Friedrich, O., Gruen, D., DeRose, J., et al. 2018, *Phys. Rev. D*, 98, 023508
 Gruen, D., Friedrich, O., Krause, E., et al. 2018, *Phys. Rev. D*, 98, 023507
 Harnois-Déraps, J. & van Waerbeke, L. 2015, *MNRAS*, 450, 2857
 Heydenreich, S., Brück, B., Burger, P., et al. 2022a, *A&A*, 667, A125
 Heydenreich, S., Brück, B., & Harnois-Déraps, J. 2021, *A&A*, 648, A74
 Heydenreich, S., Linke, L., Burger, P., & Schneider, P. 2022b, arXiv:2208.11686
 Heydenreich, S., Schneider, P., Hildebrandt, H., et al. 2020, *A&A*, 634, A104
 Heymans, C., Tröster, T., Asgari, M., et al. 2021, *A&A*, 646, A140
 Hikage, C., Oguri, M., Hamana, T., et al. 2019, *PASJ*, 71, 43
 Hoekstra, H. & Jain, B. 2008, *Annual Review of Nuclear and Particle Science*, 58, 99
 Jarvis, M., Bernstein, G., & Jain, B. 2004, *MNRAS*, 352, 338
 Joachimi, B., Lin, C. A., Asgari, M., et al. 2021, *A&A*, 646, A129
 Joachimi, B., Schneider, P., & Eifler, T. 2008, *A&A*, 477, 43
 Joachimi, B., Shi, X., & Schneider, P. 2009, *A&A*, 508, 1193
 Kacprzak, T., Kirk, D., Friedrich, O., et al. 2016, *MNRAS*, 463, 3653
 Kaiser, N. & Jaffe, A. 1997, *ApJ*, 484, 545
 Kayo, I., Takada, M., & Jain, B. 2013, *MNRAS*, 429, 344
 Kilbinger, M. & Schneider, P. 2005, *A&A*, 442, 69
 Kuijken, K., Heymans, C., Hildebrandt, H., et al. 2015, *MNRAS*, 454, 3500
 Martinet, N., Harnois-Déraps, J., Jullo, E., & Schneider, P. 2021, *A&A*, 646, A62
 Petri, A. 2016, *Astronomy and Computing*, 17, 73
 Pyne, S. & Joachimi, B. 2021, *MNRAS*, 503, 2300
 Schneider, P. 1996, *MNRAS*, 283, 837
 Schneider, P., Kilbinger, M., & Lombardi, M. 2005, *A&A*, 431, 9
 Schneider, P. & Lombardi, M. 2003, *A&A*, 397, 809
 Schneider, P., van Waerbeke, L., Jain, B., & Kruse, G. 1998, *MNRAS*, 296, 873
 Secco, L. F., Jarvis, M., Jain, B., et al. 2022, *Phys. Rev. D*, 105, 103537

- Seitz, S. & Schneider, P. 1996, *A&A*, 305, 383
Sheth, R. K. & Tormen, G. 1999, *MNRAS*, 308, 119
Springel, V., Yoshida, N., & White, S. D. M. 2001, *Nature*, 6, 79
Spurio Mancini, A., Piras, D., Alsing, J., Joachimi, B., & Hobson, M. P. 2022, *MNRAS*, 511, 1771
Takada, M. & Hu, W. 2013, *Phys. Rev. D*, 87, 123504
Takada, M. & Jain, B. 2004, *MNRAS*, 348, 897
Takahashi, R., Hamana, T., Shirasaki, M., et al. 2017, *ApJ*, 850, 24
Takahashi, R., Nishimichi, T., Namikawa, T., et al. 2020, *ApJ*, 895, 113
Takahashi, R., Sato, M., Nishimichi, T., Taruya, A., & Oguri, M. 2012, *ApJ*, 761, 152
Troxel, M. A. & Ishak, M. 2012, *MNRAS*, 419, 1804
van Waerbeke, L. 2000, *MNRAS*, 313, 524
Zürcher, D., Fluri, J., Sgier, R., Kacprzak, T., & Refregier, A. 2021, *J. Cosmology Astropart. Phys.*, 2021, 028

Table A.1: Permutations of aperture scale radii for covariance terms.

Term	permutations	Term	permutations	Term	permutations
$T_{PPP,1}$	$\theta_1\theta_4 \theta_2\theta_5 \theta_3\theta_6$	T_{BB}	$\theta_2\theta_3 \theta_4 \theta_5\theta_6 \theta_1$	$T_{PT,1}$	$\theta_1\theta_4 \theta_2\theta_3 \theta_5\theta_6$
	$\theta_1\theta_4 \theta_2\theta_6 \theta_3\theta_5$		$\theta_2\theta_3 \theta_5 \theta_4\theta_6 \theta_1$		$\theta_1\theta_5 \theta_2\theta_3 \theta_4\theta_6$
	$\theta_1\theta_5 \theta_2\theta_4 \theta_3\theta_6$		$\theta_2\theta_3 \theta_6 \theta_4\theta_5 \theta_1$		$\theta_1\theta_6 \theta_2\theta_3 \theta_4\theta_5$
	$\theta_1\theta_5 \theta_2\theta_6 \theta_3\theta_4$		$\theta_1\theta_3 \theta_4 \theta_5\theta_6 \theta_2$		$\theta_2\theta_4 \theta_1\theta_3 \theta_5\theta_6$
	$\theta_1\theta_6 \theta_2\theta_4 \theta_3\theta_5$		$\theta_1\theta_3 \theta_5 \theta_4\theta_6 \theta_2$		$\theta_2\theta_5 \theta_1\theta_3 \theta_4\theta_6$
	$\theta_1\theta_6 \theta_2\theta_5 \theta_3\theta_4$		$\theta_1\theta_3 \theta_6 \theta_4\theta_5 \theta_2$		$\theta_2\theta_6 \theta_1\theta_3 \theta_4\theta_5$
$T_{PPP,2}$	$\theta_1\theta_2 \theta_3\theta_4 \theta_5\theta_6$	$\theta_1\theta_2 \theta_4 \theta_5\theta_6 \theta_3$	$T_{PT,2}$	$\theta_3\theta_4 \theta_1\theta_2 \theta_5\theta_6$	
	$\theta_1\theta_2 \theta_3\theta_5 \theta_4\theta_6$	$\theta_1\theta_2 \theta_5 \theta_4\theta_6 \theta_3$		$\theta_3\theta_5 \theta_1\theta_2 \theta_4\theta_6$	
	$\theta_1\theta_2 \theta_3\theta_6 \theta_4\theta_5$	$\theta_1\theta_2 \theta_6 \theta_4\theta_5 \theta_3$		$\theta_3\theta_6 \theta_1\theta_2 \theta_4\theta_5$	
	$\theta_1\theta_3 \theta_2\theta_4 \theta_5\theta_6$			$\theta_1\theta_2 \theta_4\theta_5\theta_6 \theta_3$	
	$\theta_1\theta_3 \theta_2\theta_5 \theta_4\theta_6$			$\theta_1\theta_3 \theta_4\theta_5\theta_6 \theta_2$	
	$\theta_1\theta_3 \theta_2\theta_6 \theta_4\theta_5$			$\theta_2\theta_3 \theta_4\theta_5\theta_6 \theta_1$	
	$\theta_2\theta_3 \theta_1\theta_4 \theta_5\theta_6$			$\theta_4\theta_5 \theta_1\theta_2\theta_3 \theta_6$	
	$\theta_2\theta_3 \theta_1\theta_5 \theta_4\theta_6$			$\theta_4\theta_6 \theta_1\theta_2\theta_3 \theta_5$	
$\theta_2\theta_3 \theta_1\theta_6 \theta_4\theta_5$		$\theta_5\theta_6 \theta_1\theta_2\theta_3 \theta_4$			

Appendix A: List of all permutations for covariance terms

In Table A.1, we list all permutations of aperture scale radii for the terms $T_{PPP,1}$ to $T_{PT,2}$ from Sect. 3. The first permutation corresponds to the expressions in Sect. 3. The vertical dashes separate groups of scale radii, in which the terms are symmetric. These symmetries can be easily seen in the expressions in terms of the aperture mass correlation functions in Sect. 3.3.

Appendix B: Impact of shape noise on aperture mass covariance

In this section, we show that the impact of shape noise on $C_{M_{\text{ap}}^3}$ can be estimated by replacing the power spectrum $P(\ell)$ in the expressions derived in Sect. 3 by $P(\ell) + \sigma_\epsilon^2/2n$, where σ_ϵ^2 is the two-component intrinsic ellipticity dispersion and n is the galaxy number density. For this, we consider the smoothed convergence K , which is

$$K(\boldsymbol{\vartheta}) = \frac{1}{n} \sum_{i=1}^N F_\sigma(|\boldsymbol{\vartheta} - \boldsymbol{\vartheta}_i|) \kappa(\boldsymbol{\vartheta}_i), \quad (\text{B.1})$$

where F_σ is a smoothing kernel of width σ , the sum runs over the N galaxies and $\boldsymbol{\vartheta}_i$ is the position of the i th galaxy. We assume that the galaxies are distributed uniformly within the survey area A' . The kernel F_σ needs to be normalized, such that $\int_{A'} d^2\vartheta F_\sigma(\boldsymbol{\vartheta}) = 1$. As noted in van Waerbeke (2000), the smoothed convergence field K_N including shape noise can be written as

$$K_N(\boldsymbol{\vartheta}) = K(\boldsymbol{\vartheta}) + \mathcal{N}(\boldsymbol{\vartheta}) \quad \text{with} \quad \mathcal{N}(\boldsymbol{\vartheta}) = \frac{1}{n} \sum_{i=1}^N \int \frac{d^2\ell}{(2\pi)^2} \tilde{F}_\sigma(\boldsymbol{\ell}) e^{-i\boldsymbol{\ell} \cdot (\boldsymbol{\vartheta} - \boldsymbol{\vartheta}_i)} [\cos 2\phi_\ell \epsilon_1^s(\boldsymbol{\vartheta}_i) + \sin 2\phi_\ell \epsilon_2^s(\boldsymbol{\vartheta}_i)], \quad (\text{B.2})$$

where \mathcal{N} is the noise contribution, ϕ_ℓ is the polar angle of $\boldsymbol{\ell}$ and $\epsilon_{1/2}^s(\boldsymbol{\vartheta}_i)$ are the components of the intrinsic ellipticity ϵ^s of the galaxy at $\boldsymbol{\vartheta}_i$. In general, K_N has an imaginary component. However, aperture statistics, the quantity we are ultimately interested in, do not depend on the imaginary parts, which is why we concentrate on the real part here.

We now introduce a filter function U'_θ , defined such that

$$\int d^2\vartheta U'_\theta(|\boldsymbol{\alpha} - \boldsymbol{\vartheta}| K(\boldsymbol{\vartheta})) = \int d^2\vartheta U_\theta(|\boldsymbol{\alpha} - \boldsymbol{\vartheta}| \kappa(\boldsymbol{\vartheta})). \quad (\text{B.3})$$

This indicates that the aperture filter U is a convolution of U' and the smoothing kernel F_σ . Therefore, we can write Eq. (15) including shape noise with K_N as

$$\begin{aligned} \langle \hat{M}_{\text{ap}}^3 \hat{M}_{\text{ap}}^3 \rangle (\Theta_1, \Theta_2) &= \frac{1}{A^2} \int d^2\alpha_1 \int d^2\alpha_2 W_A(\alpha_1) W_A(\alpha_2) \left[\prod_{i=1}^3 \int d^2\vartheta_i U'_{\theta_i}(|\alpha_1 - \boldsymbol{\vartheta}_i|) \right] \left[\prod_{j=4}^6 \int d^2\vartheta_j U'_{\theta_j}(|\alpha_2 - \boldsymbol{\vartheta}_j|) \right] \\ &\quad \times \langle K_N(\boldsymbol{\vartheta}_i) K_N(\boldsymbol{\vartheta}_j) K_N(\boldsymbol{\vartheta}_k) K_N(\boldsymbol{\vartheta}_l) K_N(\boldsymbol{\vartheta}_m) K_N(\boldsymbol{\vartheta}_n) \rangle \\ &= \frac{1}{A^2} \int d^2\alpha_1 \int d^2\alpha_2 W_A(\alpha_1) W_A(\alpha_2) \left[\prod_{i=1}^3 \int d^2\vartheta_i U'_{\theta_i}(|\alpha_1 - \boldsymbol{\vartheta}_i|) \right] \left[\prod_{j=4}^6 \int d^2\vartheta_j U'_{\theta_j}(|\alpha_2 - \boldsymbol{\vartheta}_j|) \right] \\ &\quad \times \left\{ \langle K(\boldsymbol{\vartheta}_i) K(\boldsymbol{\vartheta}_j) K(\boldsymbol{\vartheta}_k) K(\boldsymbol{\vartheta}_l) K(\boldsymbol{\vartheta}_m) K(\boldsymbol{\vartheta}_n) \rangle \right. \\ &\quad \quad + [\langle \mathcal{N}(\boldsymbol{\vartheta}_i) \mathcal{N}(\boldsymbol{\vartheta}_j) \rangle \langle K(\boldsymbol{\vartheta}_k) K(\boldsymbol{\vartheta}_l) K(\boldsymbol{\vartheta}_m) K(\boldsymbol{\vartheta}_n) \rangle + 14 \text{ perm.}] \\ &\quad \quad + [\langle \mathcal{N}(\boldsymbol{\vartheta}_i) \mathcal{N}(\boldsymbol{\vartheta}_j) \mathcal{N}(\boldsymbol{\vartheta}_k) \mathcal{N}(\boldsymbol{\vartheta}_l) \rangle \langle K(\boldsymbol{\vartheta}_m) K(\boldsymbol{\vartheta}_n) \rangle + 14 \text{ perm.}] \\ &\quad \quad \left. + \langle \mathcal{N}(\boldsymbol{\vartheta}_i) \mathcal{N}(\boldsymbol{\vartheta}_j) \mathcal{N}(\boldsymbol{\vartheta}_k) \mathcal{N}(\boldsymbol{\vartheta}_l) \mathcal{N}(\boldsymbol{\vartheta}_m) \mathcal{N}(\boldsymbol{\vartheta}_n) \rangle \right\}, \end{aligned} \quad (\text{B.4})$$

where we used that all odd moments of the noise vanish and that \mathcal{N} and K are uncorrelated.

The expectation values are taken by averaging over all galaxy positions inside A' and taking the ensemble average. For the second-order moment of N , [van Waerbeke \(2000\)](#) showed that this leads to

$$\langle \mathcal{N}(\boldsymbol{\vartheta}) \mathcal{N}(\boldsymbol{\vartheta}') \rangle = \frac{\sigma_\epsilon^2}{2n} \int \frac{d^2\ell}{(2\pi)^2} e^{i\ell \cdot (\boldsymbol{\vartheta} - \boldsymbol{\vartheta}')} |\tilde{F}_\sigma(\ell)|^2. \quad (\text{B.5})$$

For K we find

$$\begin{aligned} \langle K(\boldsymbol{\theta}) K(\boldsymbol{\theta}') \rangle &= \left[\prod_{g=1}^N \frac{1}{A'} \int d^2\vartheta_g \right] \sum_{i=0}^N \sum_{j=0}^N F_\sigma(|\boldsymbol{\theta} - \boldsymbol{\vartheta}_i|) F_\sigma(|\boldsymbol{\theta}' - \boldsymbol{\vartheta}_j|) \langle \kappa_i \kappa_j \rangle \\ &= \frac{N(N-1)}{n^2 A'^2} \int d^2\vartheta_1 \int d^2\vartheta_2 F_\sigma(|\boldsymbol{\theta} - \boldsymbol{\vartheta}_1|) F_\sigma(|\boldsymbol{\theta}' - \boldsymbol{\vartheta}_2|) \langle \kappa_1 \kappa_2 \rangle \\ &\quad + \frac{N}{n^2 A'} \int d^2\vartheta F_\sigma(|\boldsymbol{\theta} - \boldsymbol{\vartheta}|) F_\sigma(|\boldsymbol{\theta}' - \boldsymbol{\vartheta}|) \langle \kappa^2(\boldsymbol{\vartheta}) \rangle \\ &\simeq \int d^2\vartheta_1 \int d^2\vartheta_2 F_\sigma(|\boldsymbol{\theta} - \boldsymbol{\vartheta}_1|) F_\sigma(|\boldsymbol{\theta}' - \boldsymbol{\vartheta}_2|) \langle \kappa_1 \kappa_2 \rangle + \frac{\langle \kappa^2 \rangle}{n} \int d^2\vartheta F_\sigma(|\boldsymbol{\theta} - \boldsymbol{\vartheta}|) F_\sigma(|\boldsymbol{\theta}' - \boldsymbol{\vartheta}|), \end{aligned} \quad (\text{B.6})$$

where we assumed that $N \gg 1$ and used that $\langle \kappa^2(\boldsymbol{\vartheta}) \rangle$ is the κ -correlation function at vanishing separation and thus independent of $\boldsymbol{\vartheta}$. The second summand describes the noise contribution due to the finite number of galaxies ([Schneider et al. 1998](#)). However, since $\langle \kappa^2 \rangle$ is much smaller than σ_ϵ^2 for realistic shape noise, this term is small compared to $\langle \mathcal{N}(\boldsymbol{\vartheta}) \mathcal{N}(\boldsymbol{\vartheta}') \rangle$ and we neglect it in the following. With the same approximation,

$$\langle K(\boldsymbol{\theta}_1) K(\boldsymbol{\theta}_2) K(\boldsymbol{\theta}_3) K(\boldsymbol{\theta}_4) \rangle \simeq \left[\prod_{i=1}^4 \int d^2\vartheta_i F_\sigma(|\boldsymbol{\theta}_i - \boldsymbol{\vartheta}_i|) \right] \langle \kappa_1 \kappa_2 \kappa_3 \kappa_4 \rangle \quad (\text{B.7})$$

$$\langle K(\boldsymbol{\theta}_1) K(\boldsymbol{\theta}_2) K(\boldsymbol{\theta}_3) K(\boldsymbol{\theta}_4) K(\boldsymbol{\theta}_5) K(\boldsymbol{\theta}_6) \rangle \simeq \int \left[\prod_{i=1}^6 \int d^2\vartheta_i F_\sigma(|\boldsymbol{\theta}_i - \boldsymbol{\vartheta}_i|) \right] \langle \kappa_1 \kappa_2 \kappa_3 \kappa_4 \kappa_5 \kappa_6 \rangle. \quad (\text{B.8})$$

We now assume that the width σ of the smoothing kernel is much smaller than the aperture radii θ . In that case, we can approximate the F_σ with Dirac functions, so

$$U_\theta(\vartheta) = \int d^2\vartheta' U'_\theta(|\boldsymbol{\vartheta} - \boldsymbol{\vartheta}'|) F_\sigma(\boldsymbol{\vartheta}') = \int d^2\vartheta' U'_\theta(|\boldsymbol{\vartheta} - \boldsymbol{\vartheta}'|) \delta_D(\boldsymbol{\vartheta}') = U'_\theta(\vartheta), \quad (\text{B.9})$$

and

$$\begin{aligned} \langle \hat{M}_{\text{ap}}^3 \hat{M}_{\text{ap}}^3 \rangle (\Theta_1, \Theta_2) &= \frac{1}{A^2} \int d^2\alpha_1 \int d^2\alpha_2 W_A(\alpha_1) W_A(\alpha_2) \left[\prod_{i=1}^3 \int d^2\vartheta_i U_{\theta_i}(|\alpha_1 - \boldsymbol{\vartheta}_i|) \right] \left[\prod_{j=4}^6 \int d^2\vartheta_j U_{\theta_j}(|\alpha_2 - \boldsymbol{\vartheta}_j|) \right] \\ &\quad \times \left\{ \langle \kappa_i \kappa_j \kappa_k \kappa_l \kappa_m \kappa_n \rangle + \left[\frac{\sigma_\epsilon^2}{2n} \delta_D(\boldsymbol{\vartheta}_i - \boldsymbol{\vartheta}_j) \langle \kappa_k \kappa_l \kappa_m \kappa_n \rangle + 14 \text{ perm.} \right] \right. \\ &\quad \quad + \left[\left(\frac{\sigma_\epsilon^2}{2n} \right)^2 \delta_D(\boldsymbol{\vartheta}_i - \boldsymbol{\vartheta}_j) \delta_D(\boldsymbol{\vartheta}_k - \boldsymbol{\vartheta}_l) \langle \kappa_m \kappa_n \rangle + 44 \text{ perm.} \right] \\ &\quad \quad \left. + \left[\left(\frac{\sigma_\epsilon^2}{2n} \right)^3 \delta_D(\boldsymbol{\vartheta}_i - \boldsymbol{\vartheta}_j) \delta_D(\boldsymbol{\vartheta}_k - \boldsymbol{\vartheta}_l) \delta_D(\boldsymbol{\vartheta}_m - \boldsymbol{\vartheta}_n) + 14 \text{ perm.} \right] \right\}, \end{aligned}$$

By decomposing the six- and four-point function into its connected components and considering all permutations, one can show that this is equal to the right-hand side of Eq. (16) after replacing $\langle \kappa_i \kappa_j \rangle$ by $\langle \kappa_i \kappa_j \rangle + \sigma_\epsilon^2 \delta_D(\boldsymbol{\vartheta}_i - \boldsymbol{\vartheta}_j)/2n$. This implies a power spectrum P' given by

$$\begin{aligned} P'(\ell) (2\pi)^2 \delta_D(\boldsymbol{\ell} + \boldsymbol{\ell}') &= \int d^2\vartheta_1 \int d^2\vartheta_2 \left[\langle \kappa_1 \kappa_2 \rangle + \frac{\sigma_\epsilon^2}{2n} \delta_D(\boldsymbol{\vartheta}_1 - \boldsymbol{\vartheta}_2) \right] e^{i(\boldsymbol{\ell} \cdot \boldsymbol{\vartheta}_1 + \boldsymbol{\ell}' \cdot \boldsymbol{\vartheta}_2)} \\ &= \left[P(\ell) + \frac{\sigma_\epsilon^2}{2n} \right] (2\pi)^2 \delta_D(\boldsymbol{\ell} + \boldsymbol{\ell}') , \end{aligned} \quad (\text{B.10})$$

where P is the power spectrum without shape noise. Consequently, replacing $P(\ell)$ by $P(\ell) + \sigma_\epsilon^2/2n$ in the covariance expressions from Sect. 3 gives the correct covariance for $\langle M_{\text{ap}}^3 \rangle$ in the presence of shape noise.

Appendix C: Approximation of T_{P_6}

We here derive an approximation for T_{P_6} , which is necessary to reduce the computational complexity of the covariance model. For this, we rewrite Eq. (32) as

$$\begin{aligned} T_{P_6}(\Theta_1, \Theta_2) &= \int \frac{d^2\ell_1}{(2\pi)^2} \int \frac{d^2\ell_2}{(2\pi)^2} \int \frac{d^2\ell_3}{(2\pi)^2} \int \frac{d^2\ell_4}{(2\pi)^2} \int \frac{d^2s}{(2\pi)^2} P_6(\boldsymbol{\ell}_1, \boldsymbol{\ell}_2, \boldsymbol{s} - \boldsymbol{\ell}_1 - \boldsymbol{\ell}_2, \boldsymbol{\ell}_3, \boldsymbol{\ell}_4) \\ &\quad \times \tilde{u}(\ell_1 \theta_1) \tilde{u}(\ell_2 \theta_2) \tilde{u}(|\boldsymbol{s} - \boldsymbol{\ell}_1 - \boldsymbol{\ell}_2| \theta_3) \tilde{u}(\ell_3 \theta_4) \tilde{u}(\ell_4 \theta_5) \tilde{u}(|\boldsymbol{s} + \boldsymbol{\ell}_3 + \boldsymbol{\ell}_4| \theta_6) G_A(\boldsymbol{s}) . \end{aligned} \quad (\text{C.1})$$

According to the Limber approximation (Eq. 5),

$$\begin{aligned} P_6(\boldsymbol{\ell}_1, \boldsymbol{\ell}_2, \boldsymbol{s} - \boldsymbol{\ell}_1 - \boldsymbol{\ell}_2, \boldsymbol{\ell}_3, \boldsymbol{\ell}_4) &= \left(\frac{3H_0^2 \Omega_m}{2c^2} \right)^6 \int_0^\infty d\chi \frac{q^6(\chi)}{\chi^5 a^6(\chi)} \\ &\quad \times \mathcal{P}_n^{(3d)}[\boldsymbol{\ell}_1/\chi, \boldsymbol{\ell}_2/\chi, (\boldsymbol{s} - \boldsymbol{\ell}_1 - \boldsymbol{\ell}_2)/\chi, \boldsymbol{\ell}_3, \boldsymbol{\ell}_4, (-\boldsymbol{s} - \boldsymbol{\ell}_3 - \boldsymbol{\ell}_4)/\chi; \chi] . \end{aligned} \quad (\text{C.2})$$

We now approximate $\mathcal{P}_n^{(3d)}$ under the assumption that $s \ll \ell_1, \ell_2, \ell_3, \ell_4$. This approximation is valid if G_A varies on larger scales (smaller s) than P_6 . Then, as shown by Chan et al. (2018),

$$\mathcal{P}_n^{(3d)}(\mathbf{k}_1, \mathbf{k}_2, \mathbf{q} - \mathbf{k}_1 - \mathbf{k}_2, \mathbf{k}_3, \mathbf{k}_4, -\mathbf{q} - \mathbf{k}_3 - \mathbf{k}_4; \chi) = \mathcal{P}_n^{(3d)}(\mathbf{k}_1, \mathbf{k}_2, -\mathbf{k}_1 - \mathbf{k}_2, \mathbf{k}_3, \mathbf{k}_4, -\mathbf{k}_3 - \mathbf{k}_4; \chi) + \text{additional terms} , \quad (\text{C.3})$$

where the additional terms can be calculated from the halo model. We approximate the first part of Eq. (C.3) with the 1-halo term, which is $I_6^0(k_1, k_2, k_3, k_4, k_6, \chi)$, with

$$I_n^i(k_1, \dots, k_n; \chi) = \int dm n[m, z(\chi)] b^i[m, z(\chi)] \left(\frac{m}{\bar{\rho}} \right)^n \tilde{u}_{\text{NFW}}(\mathbf{k}_1, m) \dots \tilde{u}_{\text{NFW}}(\mathbf{k}_n, m) , \quad (\text{C.4})$$

with comoving mean density $\bar{\rho}$, halo mass function $n(m, z)$ and halo bias $b(m, z)$. The \tilde{u}_{NFW} is defined as Fourier-transformation of the normalised NFW-halo profile u_{NFW} , which is

$$u_{\text{NFW}}(r, m) = \frac{1}{m} \rho(r, m) , \quad (\text{C.5})$$

where ρ is the halo density profile.

Pyne & Joachimi (2021) showed that the dominant additional term in Eq. (C.3) for $k > 0.3 h \text{ Mpc}^{-1}$ is given by a part of the 2-halo term of the pentaspectrum, so that

$$\begin{aligned} \mathcal{P}_n^{(3d)}(\mathbf{k}_1, \mathbf{k}_2, \mathbf{q} - \mathbf{k}_1 - \mathbf{k}_2, \mathbf{k}_3, \mathbf{k}_4, -\mathbf{q} - \mathbf{k}_3 - \mathbf{k}_4; \chi) &\simeq I_6^0(k_1, k_2, |\mathbf{q} - \mathbf{k}_1 - \mathbf{k}_2|, k_3, k_4, |-\mathbf{q} - \mathbf{k}_3 - \mathbf{k}_4|; \chi) \\ &\quad + P_L(q) I_3^1(k_1, k_2, |\mathbf{q} - \mathbf{k}_1 - \mathbf{k}_2|; \chi) I_3^1(k_3, k_4, |-\mathbf{q} - \mathbf{k}_3 - \mathbf{k}_4|; \chi) , \end{aligned} \quad (\text{C.6})$$

where P_L is the linear matter power spectrum. With this pentaspectrum, the last covariance part becomes

$$\begin{aligned}
T_{P_6}(\Theta_1, \Theta_2) &= \left(\frac{3H_0^2 \Omega_m}{2c^2} \right)^6 \int_0^\infty d\chi \frac{q^6(\chi)}{\chi^4 a^6(\chi)} \int \frac{d^2 \ell_1}{(2\pi)^2} \int \frac{d^2 \ell_2}{(2\pi)^2} \int \frac{d^2 s}{(2\pi)^2} \int \frac{d^2 \ell_3}{(2\pi)^2} \int \frac{d^2 \ell_4}{(2\pi)^2} \\
&\times \tilde{u}(\ell_1 \theta_1) \tilde{u}(\ell_2 \theta_2) \tilde{u}(|\mathbf{s} - \boldsymbol{\ell}_1 - \boldsymbol{\ell}_2| \theta_3) \tilde{u}(\ell_3 \theta_4) \tilde{u}(\ell_4 \theta_5) \tilde{u}(|\mathbf{s} + \boldsymbol{\ell}_3 + \boldsymbol{\ell}_4| \theta_6) G_A(\mathbf{s}) \\
&\times \left[I_6^0(\ell_1/\chi, \ell_2/\chi, |\mathbf{s} - \boldsymbol{\ell}_1 - \boldsymbol{\ell}_2|/\chi, \ell_3/\chi, \ell_4/\chi, |-\mathbf{s} - \boldsymbol{\ell}_3 - \boldsymbol{\ell}_4|/\chi; \chi) \right. \\
&\quad \left. + P_L(s/\chi) I_3^1(\ell_1/\chi, \ell_2/\chi, |\mathbf{s} - \boldsymbol{\ell}_1 - \boldsymbol{\ell}_2|/\chi; \chi) I_3^1(\ell_3/\chi, \ell_4/\chi, |-\mathbf{s} - \boldsymbol{\ell}_3 - \boldsymbol{\ell}_4|/\chi; \chi) \right] \\
&\simeq \left(\frac{3H_0^2 \Omega_m}{2c^2} \right)^6 \int_0^\infty d\chi \frac{q^6(\chi)}{\chi^4 a^6(\chi)} \int \frac{d^2 \ell_1}{(2\pi)^2} \int \frac{d^2 \ell_2}{(2\pi)^2} \int \frac{d^2 s}{(2\pi)^2} \int \frac{d^2 \ell_3}{(2\pi)^2} \int \frac{d^2 \ell_4}{(2\pi)^2} \\
&\times \tilde{u}(\ell_1 \theta_1) \tilde{u}(\ell_2 \theta_2) \tilde{u}(|\boldsymbol{\ell}_1 + \boldsymbol{\ell}_2| \theta_3) \tilde{u}(\ell_3 \theta_4) \tilde{u}(\ell_4 \theta_5) \tilde{u}(|\boldsymbol{\ell}_3 + \boldsymbol{\ell}_4| \theta_6) G_A(\mathbf{s}) \\
&\times \left[I_6^0(\ell_1/\chi, \ell_2/\chi, |\boldsymbol{\ell}_1 + \boldsymbol{\ell}_2|/\chi, \ell_3/\chi, \ell_4/\chi, |\boldsymbol{\ell}_3 + \boldsymbol{\ell}_4|/\chi; \chi) \right. \\
&\quad \left. + P_L(s/\chi) I_3^1(\ell_1/\chi, \ell_2/\chi, |\boldsymbol{\ell}_1 + \boldsymbol{\ell}_2|/\chi; \chi) I_3^1(\ell_3/\chi, \ell_4/\chi, |\boldsymbol{\ell}_3 + \boldsymbol{\ell}_4|/\chi; \chi) \right] \\
&= T_{P_6}^\infty(\Theta_1, \Theta_2) + \left(\frac{3H_0^2 \Omega_m}{2c^2} \right)^6 \int_0^\infty d\chi \frac{q^6(\chi)}{\chi^4 a^6(\chi)} \left[\int \frac{d^2 s}{(2\pi)^2} G_A(\mathbf{s}) P_L(s/\chi) \right] \\
&\times \int \frac{d^2 \ell_1}{(2\pi)^2} \int \frac{d^2 \ell_2}{(2\pi)^2} \int \frac{d^2 \ell_3}{(2\pi)^2} \int \frac{d^2 \ell_4}{(2\pi)^2} I_3^1(\ell_1/\chi, \ell_2/\chi, |\boldsymbol{\ell}_1 + \boldsymbol{\ell}_2|/\chi; \chi) I_3^1(\ell_3/\chi, \ell_4/\chi, |\boldsymbol{\ell}_3 + \boldsymbol{\ell}_4|/\chi; \chi) \\
&\times \tilde{u}(\ell_1 \theta_1) \tilde{u}(\ell_2 \theta_2) \tilde{u}(|\boldsymbol{\ell}_1 + \boldsymbol{\ell}_2| \theta_3) \tilde{u}(\ell_3 \theta_4) \tilde{u}(\ell_4 \theta_5) \tilde{u}(|\boldsymbol{\ell}_3 + \boldsymbol{\ell}_4| \theta_6) ,
\end{aligned} \tag{C.7}$$

where we used $s \ll \ell_1, \ell_2, \ell_3, \ell_4$. We refer to the last summand in this equation as $T_{P_6, 2h}$. Note that, similar to $T_{PPP, 2}$ and $T_{PT, 2}$, $T_{P_6, 2h}$ vanishes under the large-field-approximation. This can be seen by replacing $G_A(\mathbf{s})$ with $2\pi\delta_D(\mathbf{s})/A$. In this approximation, the integral in square brackets becomes zero, since $P_L(0) = 0$. Consequently, all of $T_{P_6, 2h}$ vanishes.

Appendix D: Derivation of Gaussian $\langle M_{\text{ap}}^3 \rangle$ covariance from bispectrum covariance

In this appendix, we try to use the Gaussian bispectrum covariance derived by Joachimi et al. (2009) to obtain $C_{\langle M_{\text{ap}}^3 \rangle}$. We will show that this approach only recovers the large-field approximation $T_{PPP, 1}^\infty$. In this appendix (and only here), we parameterise the bispectrum by the lengths of three $\boldsymbol{\ell}$, namely using

$$\langle \hat{\kappa}(\boldsymbol{\ell}_1) \hat{\kappa}(\boldsymbol{\ell}_2) \hat{\kappa}(\boldsymbol{\ell}_3) \rangle = (2\pi)^2 B(\ell_1, \ell_2, \ell_3) \delta_D(\boldsymbol{\ell}_1 + \boldsymbol{\ell}_2 + \boldsymbol{\ell}_3) . \tag{D.1}$$

The bispectrum covariance has been derived for Gaussian fields by Joachimi et al. (2009, see also references therein). It is

$$C_B(\ell_1, \ell_2, \ell_3; \ell_4, \ell_5, \ell_6) = \frac{(2\pi)^3 \Lambda^{-1}(\ell_1, \ell_2, \ell_3)}{A A_R(\ell_1) A_R(\ell_2) A_R(\ell_3)} [\delta_{1,4} \delta_{2,5} \delta_{3,6} + 5 \text{ permutations}] P(\ell_1) P(\ell_2) P(\ell_3) , \tag{D.2}$$

where $A_R(\ell)$ is the size of the bin of $\boldsymbol{\ell}$, defined as $A_R(\ell) = 2\pi \ell \Delta\ell$, the $\delta_{i,j}$ denote Kronecker-deltas and Λ is defined by

$$\left[\prod_{i=1}^3 \int \frac{d^2 \ell_i}{(2\pi)^2} \right] \delta_D(\boldsymbol{\ell}_1 + \boldsymbol{\ell}_2 + \boldsymbol{\ell}_3) = \int_0^\infty \frac{d\ell_1}{(2\pi)^2} \int_0^\infty \frac{d\ell_2}{(2\pi)^2} \int_0^\infty \frac{d\ell_3}{(2\pi)^2} \ell_1 \ell_2 \ell_3 2\pi \Lambda(\ell_1, \ell_2, \ell_3) . \tag{D.3}$$

We note that Eq. (D.2) was derived under the assumption that the Fourier transform $\tilde{\kappa}(\boldsymbol{\ell})$ of the convergence field is known. However, this assumption cannot be fulfilled if $\tilde{\kappa}$ is derived from the κ on only a finite survey area, as the Fourier transform formally requires κ on all of \mathbb{R}^2 . Nevertheless, we try to derive the covariance of \hat{M}_{ap}^3 from C_B . Using Eq. (9) and Eq. (D.3), the aperture statistics are

$$\langle M_{\text{ap}}^3 \rangle(\theta_1, \theta_2, \theta_3) = \left[\prod_{i=1}^3 \int \frac{d\ell_i}{2\pi} \ell_i \tilde{u}(\ell_i \theta_i) \right] B(\ell_1, \ell_2, \ell_3) \Lambda(\ell_1, \ell_2, \ell_3) . \tag{D.4}$$

We go from the continuous integration to a discrete sum in the ℓ_i , so

$$\langle M_{\text{ap}}^3 \rangle(\theta_1, \theta_2, \theta_3) = \frac{1}{(2\pi)^3} \sum_{ijk} \Delta\ell_i \Delta\ell_j \Delta\ell_k \ell_i \ell_j \ell_k \tilde{u}(\ell_i \theta_1) \tilde{u}(\ell_j \theta_2) \tilde{u}(\ell_k \theta_3) B(\ell_i, \ell_j, \ell_k) (2\pi)^3 \Lambda(\ell_i, \ell_j, \ell_k) . \tag{D.5}$$

Here, the Δl_i are the bin sizes along the l_i . Using Eq. (D.5), we derive $C_{\hat{M}_{\text{ap}}^3}$ from C_B with

$$C_{\hat{M}_{\text{ap}}^3}(\Theta_1, \Theta_2) = \frac{1}{(2\pi)^6} \sum_{ijk} \sum_{lmn} \Delta l_i \Delta l_j \Delta l_k \Delta l_l \Delta l_m \Delta l_n l_i l_j l_k l_l l_m l_n \tilde{u}(l_i \theta_1) \tilde{u}(l_j \theta_2) \tilde{u}(l_k \theta_3) \times \tilde{u}(l_l \theta_4) \tilde{u}(l_m \theta_5) \tilde{u}(l_n \theta_6) C_B(l_i, l_j, l_k; l_l, l_m, l_n) \Lambda(l_i, l_j, l_k) \Lambda(l_l, l_m, l_n). \quad (\text{D.6})$$

So the Gaussian covariance of the aperture statistics is

$$C_{\hat{M}_{\text{ap}}^3}(\Theta_1, \Theta_2) = \frac{1}{(2\pi)^6} \sum_{ijk} \sum_{lmn} \Delta l_i \Delta l_j \Delta l_k \Delta l_l \Delta l_m \Delta l_n l_i l_j l_k l_l l_m l_n \tilde{u}(l_i \theta_1) \tilde{u}(l_j \theta_2) \tilde{u}(l_k \theta_3) \times \tilde{u}(l_l \theta_4) \tilde{u}(l_m \theta_5) \tilde{u}(l_n \theta_6) \frac{(2\pi)^3 \Lambda^{-1}(l_i, l_j, l_k)}{A \Delta l_i \Delta l_j \Delta l_k l_i l_j l_k} [\delta_{i,l} \delta_{j,m} \delta_{k,n} + 5 \text{ Perm.}] \times P(l_i) P(l_j) P(l_k) \Lambda(l_i, l_j, l_k) \Lambda(l_l, l_m, l_n) = \frac{1}{(2\pi)^3 A} \sum_{ijk} \sum_{lmn} \Delta l_l \Delta l_m \Delta l_n l_l l_m l_n \tilde{u}(l_i \theta_1) \tilde{u}(l_j \theta_2) \tilde{u}(l_k \theta_3) \tilde{u}(l_l \theta_4) \tilde{u}(l_m \theta_5) \tilde{u}(l_n \theta_6) \times [\delta_{i,l} \delta_{j,m} \delta_{k,n} + 5 \text{ Perm.}] P(l_i) P(l_j) P(l_k) \Lambda(l_l, l_m, l_n). \quad (\text{D.7})$$

We evaluate the sums over the l , m , and n using the Kronecker-Deltas, so

$$C_{\hat{M}_{\text{ap}}^3}(\Theta_1, \Theta_2) = \frac{1}{(2\pi)^3 A} \sum_{ijk} \Delta l_i \Delta l_j \Delta l_k l_i l_j l_k \tilde{u}(l_i \theta_1) \tilde{u}(l_j \theta_2) \tilde{u}(l_k \theta_3) \times [\tilde{u}(l_l \theta_4) \tilde{u}(l_m \theta_5) \tilde{u}(l_n \theta_6) + 5 \text{ Perm.}] P(l_i) P(l_j) P(l_k) \Lambda(l_i, l_j, l_k). \quad (\text{D.8})$$

Finally, we go from the discrete sum back to continuous integrals (assuming $\Delta l_i \rightarrow 0$), so

$$C_{\hat{M}_{\text{ap}}^3}(\Theta_1, \Theta_2) = \frac{1}{A} \left[\prod_{i=1}^3 \int_0^\infty \frac{d l_i}{(2\pi)^2} l_i \tilde{u}(l_i \theta_i) \right] P(l_1) P(l_2) P(l_3) (2\pi)^3 \Lambda(l_1, l_2, l_3) [\tilde{u}(l_1 \theta_4) \tilde{u}(l_2 \theta_5) \tilde{u}(l_3 \theta_6) + 5 \text{ Perm.}] . \quad (\text{D.9})$$

This can also be written as

$$C_{\hat{M}_{\text{ap}}^3}(\Theta_1, \Theta_2) = \frac{1}{A} \left[\prod_{i=1}^3 \int \frac{d^2 l_i}{(2\pi)^2} \tilde{u}(l_i \theta_i) \right] P(l_1) P(l_2) P(l_3) (2\pi)^2 \delta_{\text{D}}(\mathbf{l}_1 + \mathbf{l}_2 + \mathbf{l}_3) [\tilde{u}(l_1 \theta_4) \tilde{u}(l_2 \theta_5) \tilde{u}(l_3 \theta_6) + 5 \text{ Perm.}] \quad (\text{D.10}) = \frac{1}{A} \int \frac{d^2 l_1}{(2\pi)^2} \int \frac{d^2 l_2}{(2\pi)^2} \tilde{u}(l_1 \theta_1) \tilde{u}(l_2 \theta_2) \tilde{u}(|\mathbf{l}_1 + \mathbf{l}_2| \theta_3) P(l_1) P(l_2) P(|\mathbf{l}_1 + \mathbf{l}_2|) \times [\tilde{u}(l_1 \theta_4) \tilde{u}(l_2 \theta_5) \tilde{u}(|\mathbf{l}_1 + \mathbf{l}_2| \theta_6) + 5 \text{ Perm.}] .$$

By comparing with Eq. (43) we see that this expression corresponds to $T_{PPP,1}^\infty$, which is the Gaussian covariance of \hat{M}_{ap}^3 in the limiting case of large survey areas A . The term $T_{PPP,2}$ is not recovered from the bispectrum covariance. This is a direct consequence of the assumption that $\tilde{\kappa}(\mathbf{l})$ can be reconstructed from the κ on the finite survey window A in the derivation of Eq. (D.2). This assumption is equivalent to assuming a window function W_A , which is one on the whole \mathbb{R}^2 , leading to the large-field approximation for G_A in Eq. (42). This approximation directly reduces $T_{PPP,1}$ to $T_{PPP,1}^\infty$ and $T_{PPP,2}$ to zero.